

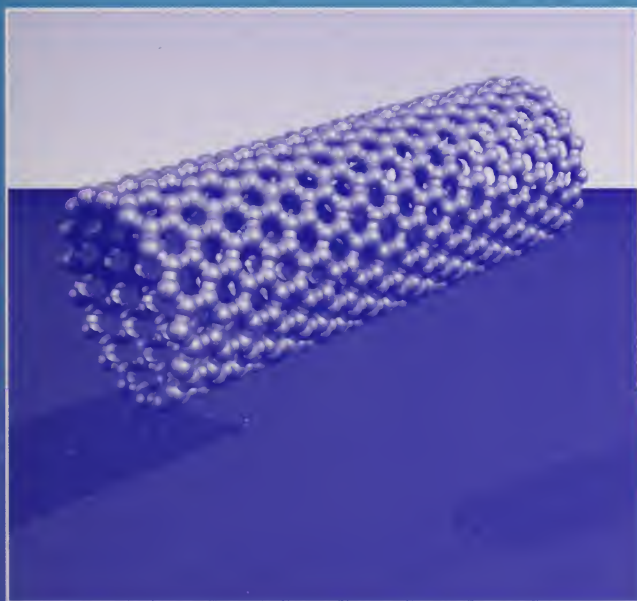
NATL INST. OF STAND & TECH



A11107 017406

NIST  
PUBLICATIONS

# Measurement Issues in Single Wall Carbon Nanotubes



Stephen Freiman  
Stephanie Hooker  
Kalman Migler  
Sivaram Arepalli

**NIST**

National Institute of  
Standards and Technology  
U.S. Department of Commerce

Special  
Publication  
960-19

QC  
100  
.457  
#960-19  
2008  
C.2



Special Publication 960-19

# Measurement Issues in Single Wall Carbon Nanotubes

Edited by:

Stephen Freiman

Stephanie Hooker

Kalman Migler

NIST Materials Science and  
Engineering Laboratory

and

Sivaram Arepalli

NASA-DSC

March 2008



U.S. Department of Commerce

Carlos M. Gutierrez, Secretary

National Institute of Standards and Technology

Dr. James M. Turner, Acting Director and Deputy Director

Certain equipment, instruments or materials are identified in this paper in order to adequately specify the experimental details. Such identification does not imply recommendation by the National Institute of Standards and Technology nor does it imply the materials are necessarily the best available for the purpose.

Official contribution of the National Institute of Standards and Technology; not subject to copyright in the United States.

---

National Institute of Standards and Technology

Special Publication 960-19

Natl. Inst. Stand. Technol.

Spec. Publ. 960-19

78 pages (March 2008)

CODEN: NSPUE2

U.S. GOVERNMENT PRINTING OFFICE

WASHINGTON: 2001

**For sale by the Superintendent of Documents**

**U.S. Government Printing Office**

Internet: [bookstore.gpo.gov](http://bookstore.gpo.gov) Phone: (202) 512-1800 Fax: (202) 512-2250

Mail: Stop SSOP, Washington, DC 20402-0001

## **FORWORD**

The NIST Recommended Practice Guide on Measurement Issues in *Single Wall Carbon Nanotubes* represents the output from the 2nd NASA-NIST workshop devoted to issues of nanotube purity, dispersion and measurement techniques held at NIST in 2005. In attendance were over 80 participants, representing private corporations, universities, and government laboratories. The primary purpose of the workshop was to bring together technical and business leaders in the field of single wall carbon nanotubes (SWNTs) to discuss measurement priorities and aid in the development of measurement protocols. This guide lays out written protocols to enable product developers to more rapidly assess as-received materials, prepare quality nanotube dispersions, and ultimately achieve both repeatability and high performance in their resulting value-added devices. The technical chapters in this guide were written by leading practitioners in the field and present standard methods currently used for characterization of single wall nanotubes in a straightforward fashion.

- 1. Introduction**
- 2. Thermogravimetric Analysis by Sivaram Arepalli and Pavel Nikolaev, NASA JSC**
- 3. Near-IR Spectroscopy by Robert Haddon and Mikhail Itkis, University of California, Riverside**
- 4. Raman Spectroscopy by Anna Swan, Boston University**
- 5. Optical, Electron, and Scanned Probe Microscopy by Cheol Park and Peter Lillehei, NASA Langley Research Center, Science and Technology Corporation Hampton, VA, and National Institute of Aerospace, VA**

A free download of this Recommended Practice Guide and more Information on the SP 960 series can be found at: <http://www.nist.gov/practiceguides>. This web site includes a complete list of NIST Practice Guides and ordering information.



- 1. Introduction**
- 2. Thermogravimetric Analysis (TGA)**
  - 2.1. General Description
  - 2.2. Types of TGA Instruments
  - 2.3. Operating Principle and Definitions
  - 2.4. Sources of Uncertainty
  - 2.5. Practical Concerns
    - 2.5.1. Material Inhomogeneity
    - 2.5.2. Combustion
    - 2.5.3. Heating Rate
    - 2.5.4. Sample Mass
  - 2.6. Suggested Protocol
  - 2.7. Appendix
    - 2.7.1. Protocol Development
    - 2.7.2. Material Inhomogeneity
    - 2.7.3. Heating Rate
    - 2.7.4. Sample Compaction
- 3. Near-Infrared (NIR) Spectroscopy**
  - 3.1. Introduction
  - 3.2. Formulation of Method: Electronic Structure and Optical Spectroscopy of SWNTs
  - 3.3. Practical Procedure
    - 3.3.1. Choice of Spectrophotometer
    - 3.3.2. Sample Preparation
    - 3.3.3. Practical Example of Spectral Measurements and Relative Purity Calculations
    - 3.3.4. Most Common Source of Experimental Uncertainty: Distorted Baseline
  - 3.4. Characterization of NIR method
    - 3.4.1. Reproducibility of the Purity Evaluation
    - 3.4.2. Influence of Light Scattering
    - 3.4.3. Influence SWNT Concentration on Relative Purity Determination
  - 3.5. Examples of the Application of NIR Purity Evaluation Procedure
    - 3.5.1. Optimization of SWNT Synthesis
    - 3.5.2. Evaluation of Efficiency of Purification and Optimization of Purification
  - 3.6. Frequently Asked Questions about the Capabilities and limitations of the NIR



#### **4. Raman Spectroscopy**

- 4.1. Resonant Raman Scattering in Carbon Nanotubes
- 4.2. Raman-Active Modes in Carbon Nanotubes (RBM, D, G and G')
  - 4.2.1. Radial breathing mode (RBM)
  - 4.2.2. The G band
  - 4.2.3. Second Order Raman Scattering, the D and G' Modes (Zone Boundary Phonons)
- 4.3. Width of the Resonance
- 4.4. Strength of the Raman Signal; Electron-Phonon Coupling
  - 4.4.1. Depolarization and Selection Rules
- 4.5. Practical Considerations
  - 4.5.1. Measurement Setup
  - 4.5.2. Laser Power Heating Effects
  - 4.5.3. Material Inhomogeneity
- 4.6. Appendix
  - 4.6.1. Illustration of Aggregation Effects
  - 4.6.2. Illustration of Heating Effects
  - 4.6.3. Measurements from One Individual Nanotube - "Nano-Slit Effect"

#### **5. Optical, Electron and Probe Microscopy**

- 5.1. General Description
- 5.2. Introduction
- 5.3. Experimental Description
  - 5.3.1. Instrumentation
  - 5.3.2. Contrast generation
- 5.4. Conclusions

#### **6. Summary**



## 1 Introduction

Single-walled carbon nanotubes (SWNTs) are the most promising of all nanomaterials, with unique electronic and mechanical properties which lend themselves to a variety of applications, such as field-emission displays, nanostructured composite materials, nanoscale sensors, and elements of new nanoscale logic circuits (1-5). In all cases the quality of the SWNT material is important, and for some applications it is paramount. Despite sustained efforts, all currently known SWNT synthetic techniques, generate significant quantities of impurities, such as amorphous and graphitic forms of carbon and carbon encapsulated catalytic metal nanoparticles. The presence of such impurities necessitates the application of vigorous purification procedures, which adds to the high cost of production and limits the application of these materials.

Improvements in SWNT quality by optimization of the synthesis, as well as subsequent purification steps is a multi-parametric task which requires the accurate and efficient evaluation of small changes in the purity and yield of bulk quantities of the SWNT product as a function of the synthetic parameters and purification protocol. Ideally, such a procedure should provide a rapid, convenient, and unambiguous measure of the bulk purity of standard SWNT samples with instrumentation that is routinely available in research laboratories. For customers and end users of SWNTs such an evaluation procedure is essential for the development of quality assurance measures which allow a comparison of commercial materials with customer determined specifications.

While the reader may believe that this is a settled issue because many suppliers label their SWNT products with percentage purities, evaluation of such samples shows that in many cases the purity is overstated - some to a high degree (6). Progress in chemistry and material science has been marked by the ability to obtain pure substances: the isolation of the pure elements and the refinements that have occurred in electronics grade silicon are obvious examples. While it may not be possible to obtain analytically pure SWNTs, the nanotechnology industry will benefit greatly from a serious attempt to specify the quality of nanotube containing materials, both in the research and commercialization stages.

In this Practice Guide we present a number of analytical techniques which are relevant to the evaluation of the purity of SWNT materials. There are two major forms of impurities in current SWNT preparations: the metal catalyst residue and the carbonaceous component which usually takes the form of amorphous carbon and nanographitic structures. Most of the analytical techniques discussed in this Guide are suited to the detection of only one of those fractions, and the choice of an analytical technique is critical(7). In special cas-

es, such as the comprehensive characterization of the highest purity reference materials for standards development, the application of a number of analytical techniques is required (8).

In Chapter 2 we discuss Thermo-Gravimetric Analysis (TGA) which is the most efficient tool for determining the metallic impurities in SWNT material. In certain special cases the TGA technique is also capable of providing information on the carbonaceous impurities as a result of differences in combustion temperatures.

The evaluation of the purity of the carbonaceous component of SWNT material is a long-standing problem, which has traditionally been addressed at a local scale by Scanning Electron Microscopy (SEM) and Transmission Electron Microscopy (TEM) techniques. (7) Recently, Near Infrared (NIR) Spectroscopy has been advanced as an efficient tool to measure the carbonaceous purity of bulk SWNT samples and is discussed in Chapter 3. The NIR technique takes advantage of the unique spectroscopic features resulting from the interband electronic transitions in SWNTs and it is most efficient for SWNT samples with a narrow distribution of diameters; it is distinguished from other methods because it is quantitative and readily applicable to bulk samples. The power of this method is already established by published studies that document the improvements in synthetic parameters and purification protocols that may be achieved by its application.

Chapter 4 discusses the application of resonantly enhanced Raman spectroscopy for SWNT purity evaluation. The two most prominent features observed in the first-order resonant Raman spectrum of SWNTs are the low frequency radial breathing mode (RBM) and the high frequency G-band; the D-band associated with disordered carbon provides a measure of the contribution of carbonaceous impurities. A comparison of the intensities of the RBM- or G-bands to the intensity and shape of the D-band provides information on the SWNT content of the sample. Due to the resonant nature of the SWNT Raman response, multiple excitation wavelengths must be utilized in order to allow for the contributions of SWNTs of different diameters.

Chapter 5 discusses the application of optical, electron and scanning probe microscopy (SPM) for SWNT quality evaluation. TEM and SEM have traditionally been the most important techniques for the characterization of carbon nanotubes. Indeed, SWNTs were discovered in 1993 using TEM, and high-resolution TEM remains a major analytical tool for the study of SWNT nucleation and growth. The SEM technique has been extensively used to monitor the efficiency of the bulk scale production of SWNTs by a variety of synthetic

techniques, and it has traditionally been the most popular tool to evaluate the quality of as-prepared SWNT soot. (7) Because a typical SEM frame visualizes less than  $10^{-12}$  g of an inhomogeneous sample for which there is no published algorithm with which to quantify the SWNT content, the use of these techniques to assess the purity of bulk SWNT samples is not recommended.

### Literature Cited

1. Zhou O, Shimoda H, Gao B, Oh SJ, Fleming L, Yue GZ. 2002. *Accounts of Chemical Research* 35:1045-53
2. Mamedov AA, Kotov NA, Prato M, Guldi DM, Wicksted JP, Hirsch A. 2002. *Nature Materials* 1:257
3. Kong J, Franklin NR, Zhou CW, Chapline MG, Peng S et al. 2000. *Science* 287:622-5
4. Avouris P. 2002. *Accounts of Chemical Research* 35:1026-34
5. Dai HJ. 2002. *Accounts of Chemical Research* 35:1035-44
6. Giles J. 2004. *Nature* 432:791
7. Itkis ME, Perea DE, Niyogi S, Love J, Tang J et al. 2004. *Journal of Physical Chemistry B* 108:12770-5
8. Arepalli S, Nikolaev P, Gorelik O, Hadjiev VG, Bradley HA et al. 2004. *Carbon* 42:1783-91

## **2. THERMOGRAVIMETRIC ANALYSIS (TGA)**

**Sivaram Arpalli and Pavel Nikolaev**

**NASA-DSC**

### **2.1. General Description**

Thermogravimetric analysis (TGA) is an analytical technique used to determine a material's thermal stability and its fraction of volatile components by monitoring the change in mass that occurs as a specimen is heated [1-4]. The measurement is normally carried out in air or in an inert atmosphere, such as Helium or Argon, and the mass is recorded as a function of increasing temperature. Sometimes, the measurement is performed in a lean oxygen atmosphere ((1 to 5) %  $O_2$  in  $N_2$  or He) to slow down oxidation [5]. In addition to mass changes, some instruments also record the temperature difference between the specimen and one or more reference pans (differential thermal analysis, or DTA) or the heat flow into the specimen pan compared to that of the reference pan (differential scanning calorimetry, or DSC). The latter can be used to monitor the energy released or absorbed via chemical reactions during the heating process. In the particular case of carbon nanotubes, the mass change in an air atmosphere is typically a superposition of the mass loss due to oxidation of carbon into gaseous carbon dioxide and the mass gain due to oxidation of residual metal catalyst into solid oxides [6-8].

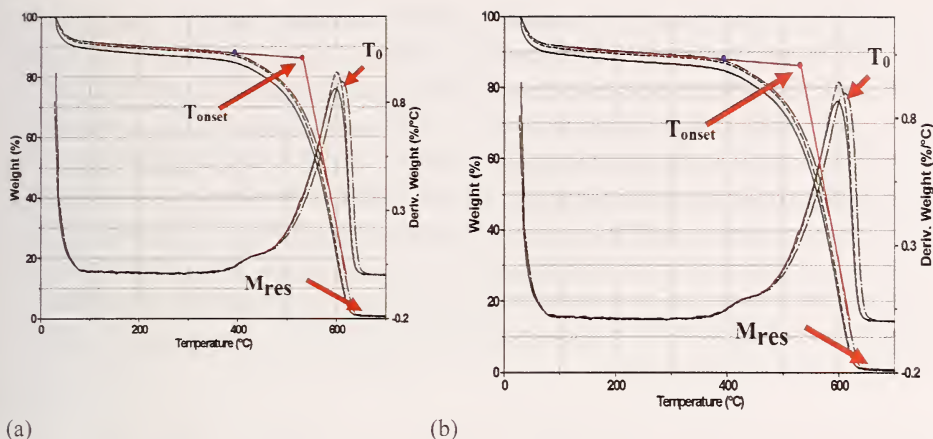
### **2.2. Types of TGA Instruments**

TGA instruments can be divided into two general types: vertical and horizontal balance. Vertical balance instruments have a specimen pan hanging from the balance or located above the balance on a sample stem. It is necessary to calibrate these instruments in order to compensate for buoyancy effects due to the variation in the density of the purge gas with temperature, as well as the type of gas. Vertical balance instruments which do not have reference pans are incapable of true DTA or DSC measurements. Horizontal balance instruments normally have two pans (sample and reference) and can perform DTA and DSC measurements. They are considered free from buoyancy effects, but require calibration to compensate for differential thermal expansion of balance arms. One common instrument for general purpose use, the TA Instruments Model SDT 2790, is used as an example for the following description and discussion [2].

### **2.3. Operating Principle and Definitions**

In most cases, TGA analysis is performed in an oxidative atmosphere (air or oxygen and inert gas mixtures) with a linear temperature ramp (temperature of sample, T). The maximum temperature is selected so that the specimen mass





**Figure 2.1:** (a) TGA of purified SWCNTs; 3 specimens sampled from the same batch. (b) Graph illustrating the ambiguity in determining  $T_{\text{onset}}$ . (Plots are generated by instrument software which report values in weight.)

is stable at the end of the experiment, implying that all chemical reactions are completed (i.e., all of the carbon is burnt off leaving behind metal oxides). This approach provides two important numerical pieces of information: ash content (residual mass,  $M_{\text{res}}$ ) and oxidation temperature ( $T_0$ ) (Figure 2.1). While the definition of ash content is unambiguous, oxidation temperature can be defined in many ways, including the temperature of the maximum in the mass loss rate ( $dm/dT_{\text{max}}$ ) and the mass loss onset temperature ( $T_{\text{onset}}$ ). The former refers to the temperature of the maximum rate of oxidation, while the latter refers to the temperature when oxidation just begins. The use of the former definition,  $T_0 = dm/dT_{\text{max}}$ , is preferred for two reasons. First, due to the gradual initiation of transition (sometimes up to 100 °C, Figure 2.1) it may be difficult to determine  $T_{\text{onset}}$  precisely. Gradual onset is believed to be due to nanotubes being contaminated with amorphous carbon and other types of carbonaceous impurities that oxidize at temperatures lower than that of nanotubes. In these cases,  $T_{\text{onset}}$  describes the properties of the impurities rather than the nanotubes. Second, mass loss due to carbon oxidation is often superimposed on the mass increase due to catalyst oxidation at low temperatures [1]. In some cases this leads to an upward swing of the TGA curve prior to the bulk of the mass loss, which makes the definition of  $T_{\text{onset}}$  even more difficult and ambiguous. However, determining  $dm/dT_{\text{max}}$  is relatively straightforward. Therefore, oxidation temperature is herein defined as  $T_0 = dm/dT_{\text{max}}$ .

TGA measurement of “as-produced” nanotube material in air usually produces only one peak in the  $dm/dT$  curve, as “fluffy” raw nanotubes oxidize rapidly in an oxygen-rich environment. However, analysis of purified nanotube material

in air may produce more than one peak. These additional peaks are likely due to the fact that purified material contains a fraction of nanotubes with damage and/or with functional groups (i.e., the material is oxidized at lower temperatures) or because purified material is more compacted after drying. The position of each peak is also strongly affected by the amount and morphology of the metal catalyst particles and other carbon-based impurities, as well as their distribution within a specimen. A lean oxygen environment can be used to better separate these peaks. In addition, these peaks have also been attributed to various components in the nanotube material (amorphous carbon, nanotubes, graphitic particles), and it may be possible to quantify these components by deconvolution of peaks [5].

Oxidation temperature, is basically a measure of the thermal stability of nanotubes in air and depends on a number of parameters. For example, smaller diameter nanotubes are believed to oxidize at lower temperature due to a higher curvature strain. Defects and derivatization moiety in nanotube walls can also lower the thermal stability. Active metal particles present in the nanotube specimens may catalyze carbon oxidation, so the amount of metal impurity in the sample can have a considerable influence on the thermal stability. It is impossible to distinguish these contributions, but, nevertheless, thermal stability is a good measure of the overall quality of a given nanotube sample. Higher oxidation temperature is always associated with purer, less-defective samples [6].

### **2.4. Sources of Error**

When performing TGA runs on especially clean nanotubes with minimal ash content ( $< 3\%$ ), it should be noted that residual mass is sometimes negative. This happens even after fresh calibration of the instrument. The long-term stability of the instrument zero (over a 3 h run) is within (20 to 40)  $\mu\text{g}$ , which constitutes (1 to 2) % of the initial (2 to 4) mg sample. For samples with very small ash content, this amounts to a fairly large uncertainty. It is therefore necessary to weigh each ash residue independently using a microbalance. This way ash content measurement accuracy is greatly improved. Other instruments may have better long-term zero stability, but it is still preferable to check ash content occasionally by independent measurement. Additionally, there may be a time lag in the sample temperature and the oven temperature which can be reduced by lowering the ramp rates. Finally, temperature calibration should be done periodically according to the instrument manufacturer's specifications.

### **2.5 Practical Concerns**

#### **2.5.1 Material Inhomogeneity**

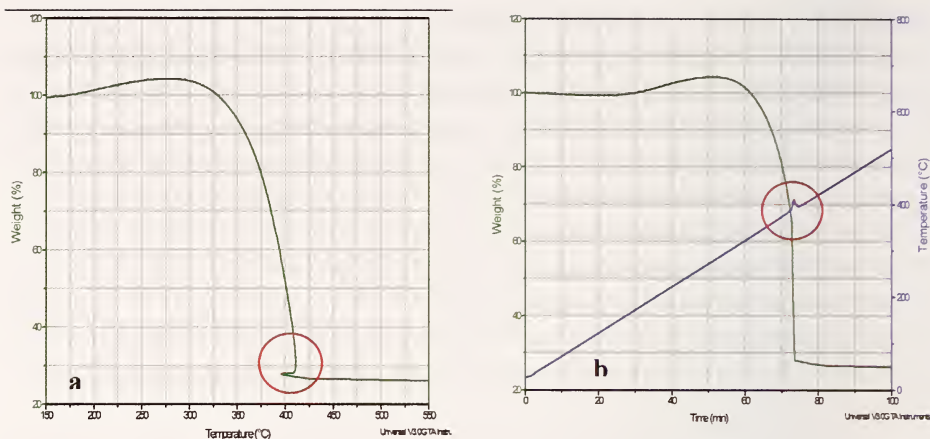
It has been noted that when TGA measurements are performed on several nanotube specimens sampled from the same batch, the TGA traces do not necessarily

ily coincide (Figures 2.1 to 2.8). There is always some variation that exceeds the accuracy and repeatability of the instrument. This observation serves to emphasize that carbon nanotube batches are not pure chemicals and, therefore, are not as homogenous and uniform as is usually implied for pure chemicals. This means that values of  $M_{res}$  and  $T_o$  produced in one TGA run are not necessarily representative of the whole batch. The only reasonable approach to this problem is to perform TGA on at least three (or more) specimens sampled from the batch and calculate mean averages of  $M_{res}$  and  $T_o$ . Interestingly, this approach also allows one to calculate standard deviations of  $M_{res}$  and  $T_o$ . It is obvious that standard deviations  $\sigma_{M_{res}}$  and  $\sigma_{T_o}$  can serve as a measure of the inhomogeneity of the nanotubes in the batch (See appendix for experimental data and discussion).

### 2.5.2 Combustion

Sometimes a strange, and unexpected, effect is observed in the TGA results (Figure 2.2). The mass trace suddenly goes *backwards* along the abscissa and then continues forward as usual. This behavior becomes easily explainable if the mass trace and the temperature are plotted versus *time*. In this graph, it is evident that the event is accompanied by a sudden loss of a significant fraction of the sample mass, as well as a large spike in the temperature difference (DTA) plot. At the same time, temperature goes up by (10 to 20) °C, and then comes down and continues along a linear ramp. We have estimated that the temperature increase rate reaches up to 50 °C/min during such events and is fairly independent of the nominal furnace heating rate. These are unambiguous signs of combustion (i.e., the sample starts burning and releases a considerable amount of heat very quickly, causing a sharp increase in temperature followed by heat dissipation and a subsequent temperature drop). This behavior is more often observed on as-produced unpurified nanotubes that are “fluffy” and have more metal catalyst. It is noticed that combustion decreases  $M_{res}$  and increases its standard deviation. This probably happens due to ejection of smoke particulates from the sample pan during rapid burning (i.e., there is some poorly controlled mass loss beyond oxidation of carbon). Therefore it is better to avoid conditions that cause combustion.





**Figure 2.2:** Evidence of nanotube combustion in TGA. (a) Trace going “backward”. (b) Temperature spike caused by combustion. Note different abscissa units – temperature on (a) and time on (b).

## 2.5.3 Heating Rate

Typical heating rates employed in TGA measurements of carbon nanotube specimens are in the (10 to 20) °C/min range. It has been noted that heating rate has a pronounced effect on the measured values of  $M_{res}$  and  $T_0$  and their standard deviations (see Appendix). The effect on  $T_0$  has been attributed in the literature to the limited rate of heat conduction into the sample. The effect on  $M_{res}$  is mostly related to combustion that higher ramp rates are more likely to produce. It is found that in as-produced unpurified (“fluffy”) samples, combustion is likely to occur at or above 5 °C/min. The conclusion is that heating rate must be constant in all measurements to avoid inconsistency in  $T_0$  measurement, and at or below 5 °C/min to avoid combustion. Selecting a heating rate of 5 °C/min is a reasonable compromise, considering that lowering the rate more causes unacceptably long experiments.

## 2.5.4 Sample Mass

When working with as-produced “fluffy” nanotubes, it is difficult to place more than 2 to 4 mg of material into a typical 200  $\mu$ L sample pan. Considering the stability of modern TGA instruments, this quantity of material is still acceptable, but should be an absolute minimum. Samples of approximately 10 mg are recommended.

## 2.6 Suggested Protocol

Based on the discussion above and results of the study reported in the Appendix (Section 2.7), the following protocol for TGA measurements is proposed.

If this protocol is followed for each sample, it will produce results that can be cross-compared.

1. Heating rate 5 °C/min. in air. Maximum temperature sufficient to stabilize sample mass (typically 800 °C).
2. Sample size at least (2 to 4) mg, more if possible.
3. Three separate TGA runs on each sample.
4. Ash content measured independently on microbalance.

Mean values of  $T_o$  and  $M_{res}$  are representative of the sample oxidation temperature and ash content. Standard deviations of  $T_o$  and  $M_{res}$  are representative of the sample inhomogeneity.

## 2.7 Appendix

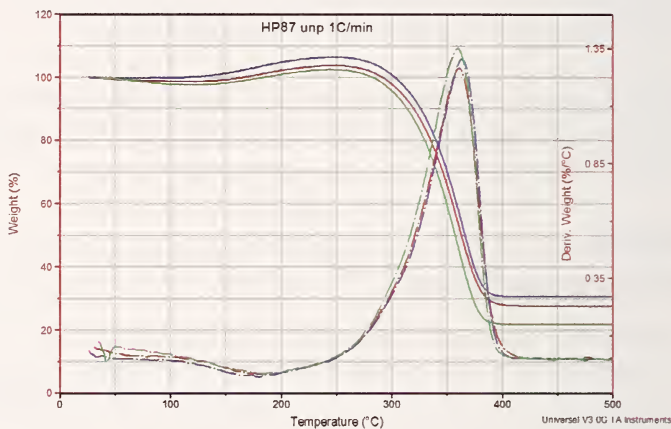
### 2.7.1 Protocol Development

All TGA experiments were performed using a TA Instruments SDT 2790 TGA with air as a purge gas at a flow rate of  $10^{-4} \text{ m}^3/\text{min}$  (100 sccm). Figures 2.1 to 2.9 were generated by this instrument. All samples were from the same batch of as-produced (“fluffy”) single-wall carbon nanotubes produced by a high-pressure carbon monoxide process (HiPco). The inhomogeneity of the material, the heating rate, combustion, and their combined effect on the results of the TGA experiments were studied. In addition, we investigated the stability of the instrument zero and its implications in determining precise ash content.

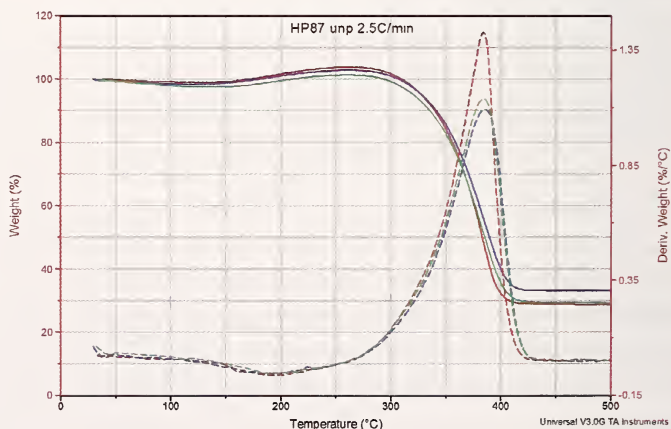
### 2.7.2 Material Inhomogeneity

Each nanotube specimen was analyzed via TGA three times at each of following heating rates: (1, 2.5, 5, 10, 30 and 100) °C/min. TGA traces for these experiments are shown on Figures 3 through 8. One can observe that for any given set of experimental parameters, the shape of the TGA curve, as well as the oxidation temperature,  $T_o$ , and ash content,  $M_{res}$ , vary in each run. Variations in  $T_o$  can exceed (10 to 20) °C, and variations in  $M_{res}$  can exceed 5 % of the initial sample mass (i.e., these variations are quite significant and cannot be dismissed as an instrument error). These variations are likely due to the inhomogeneity of the starting material. Therefore, ash content and oxidation temperature of the nanotube batch as a whole are best described as a mean of results from at least three runs. As each run takes considerable time ( $\approx 3 \text{ h}$  at 5 °C/min heating rate) and consumes (2 to 4) mg of the sample, it is impractical to do more than three runs. A sample size of (2 to 4) mg is sufficient to produce good data, but not too large as to consume a significant fraction of the nanotube material available. It has also been noticed that nanotube materials of different properties have varying standard deviations of  $T_o$  ( $\sigma_T$ ) and  $M_{res}$  ( $\sigma_M$ ). This

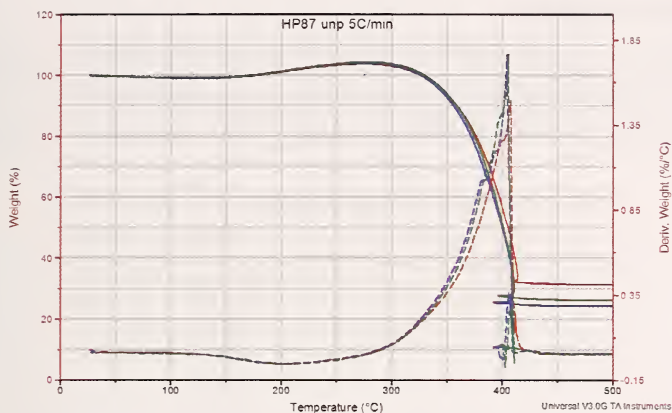
result could also be due to the varying degree of inhomogeneity in different samples. For example, unpurified and purified nanotubes can have  $\sigma_T \approx 2.7^\circ\text{C}$  and  $\sigma_T \approx 6.5^\circ\text{C}$  respectively ( $5^\circ\text{C}/\text{min}$  heating rate). Therefore,  $\sigma_M$  and  $\sigma_T$  values can be used to describe inhomogeneity of the sample – the larger the standard deviation, the more inhomogeneous the sample.



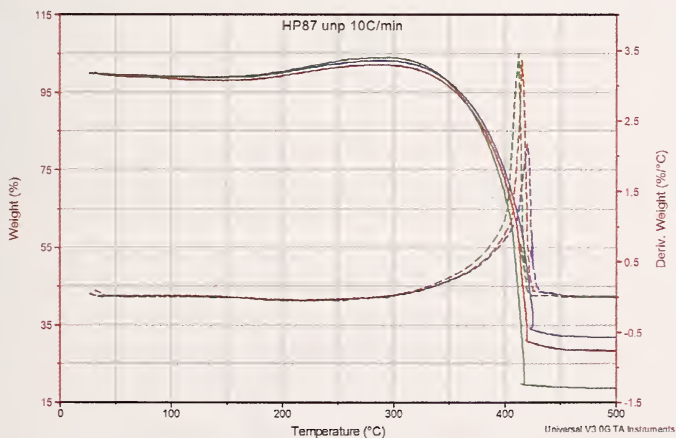
**Figure 2.3:** TGA graphs of an unpurified SWCNT material; three specimens sampled from the same batch;  $1^\circ\text{C}/\text{min}$  heating rate in air.



**Figure 2.4:** TGA graphs of an unpurified SWCNT material; three specimens sampled from the same batch;  $1^\circ\text{C}/\text{min}$  heating rate in air.



**Figure 2.5:** TGA graphs of an unpurified SWCNT material; three specimens sampled from the same batch; 5 °C/min heating rate in air.

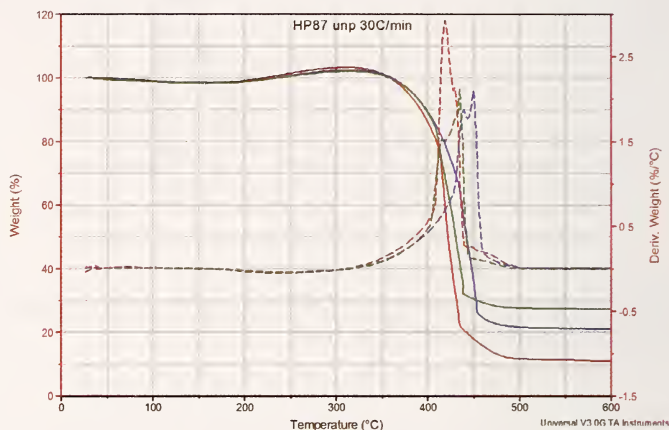


**Figure 2.6:** TGA graphs of an unpurified SWCNT material; three specimens sampled from the same batch; 10 °C/min heating rate in air.



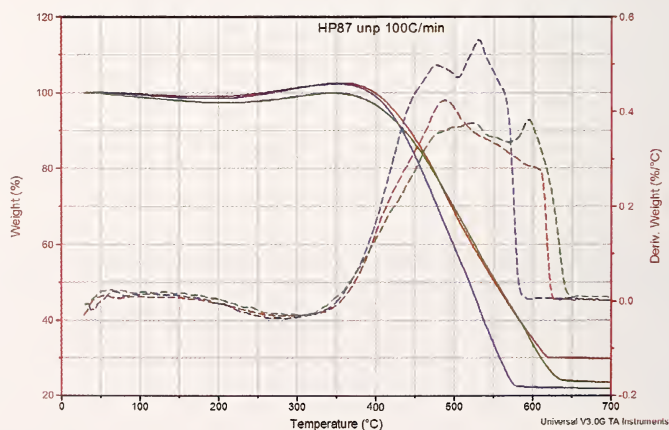
### 2.7.3 Heating Rate

Heating rates as high as 100 °C/min and as low as 1 °C/min are reported in the literature. As mentioned above, we have done experiments with the following heating rates: (1, 2.5, 5, 10, 30 and 100) °C/min. Figure 2.9 shows that the

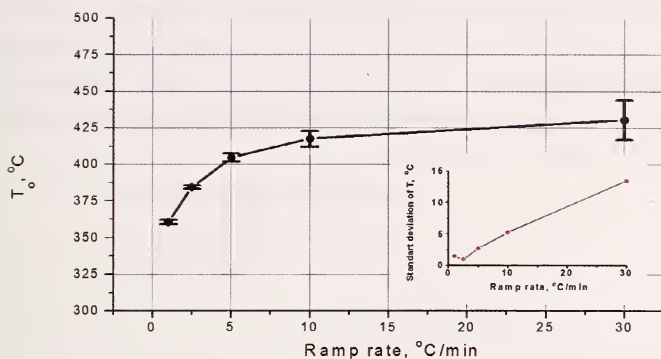


**Figure 2.7:** TGA graphs of an unpurified SWCNT material; three specimens sampled from the same batch; 30 °C/min heating rate in air.

mean value of  $T_0$  increases gradually from (360 to 430) °C as the heating rate increases from 1 °C/min to 30 °C/min. It is difficult to reliably determine  $T_0$  (and its standard deviation) for the experiment with a 100 °C/min heating rate



**Figure 2.8:** TGA graphs of an unpurified SWCNT material; three specimens sampled from the same batch; 100 °C/min heating rate in air.

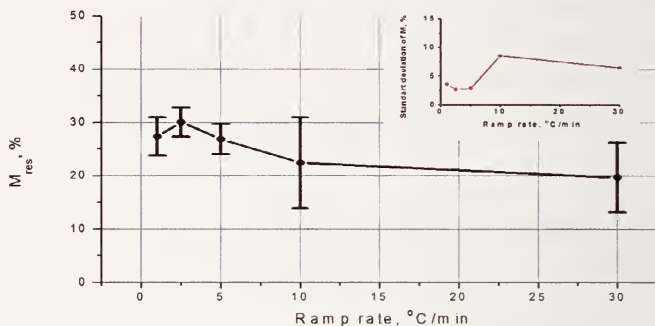


**Figure 2.9:** Heating rate dependence of oxidation temperature,  $T_o$ , and its standard deviation  $\sigma_{T_o}$  (inset).

(Figure 2.8) due to the very broad transition with several peaks that are not reproducible (this will be discussed later). The origin of such a significant change in  $T_o$  (70  $^{\circ}\text{C}$ ) is usually attributed to the limited rate of heat conduction into the sample. It is important to emphasize that  $T_o$  depends on the heating rate, and, therefore, its values produced at different heating rates cannot be directly compared to each other. The inset in Figure 2.9 shows that the standard deviation of  $T_o$  also increases significantly as the heating rate increases, varying from (1 to 13.5)  $^{\circ}\text{C}$ .

The value of  $M_{\text{res}}$  and its standard deviation are also dependent on the heating rate. Figure 2.10 shows that  $M_{\text{res}}$  for (1, 2.5 and 5)  $^{\circ}\text{C}/\text{min}$  heating rates are well within one standard deviation (which is nearly constant), while above 5  $^{\circ}\text{C}/\text{min}$ ,  $M_{\text{res}}$  becomes significantly smaller and its standard deviation sharply increases. This observation can be explained by spontaneous combustion of the nanotubes above 5  $^{\circ}\text{C}/\text{min}$  heating rate (i.e., the heat released in the exothermic reaction is enough to sustain rapid burning of the sample). It is impossible to confirm this by direct observation of the sample in the TGA furnace, but the observed behavior of  $T_o$  and  $M_{\text{res}}$  also points in this direction. Combustion, unlike slow oxidation, is an uncontrollable process, strongly dependent on the morphology and size of a particular specimen. Combustion releases particulate matter (smoke) from the sample in a relatively random fashion, therefore reducing residual mass, which is indeed observed above 5  $^{\circ}\text{C}/\text{min}$  as discussed above (Figure 2.10). A large increase in the standard deviation of  $M_{\text{res}}$  is also consistent with this explanation, as the additional mass loss due to smoke release in a particular run can vary significantly with the size and morphology of the specimen. In the absence of combustion,  $T_o$  must depend only on the properties of the nanotube specimen. On the other hand, when the heating rate is

fast enough to produce combustion, the peak in the  $dM/dt$  is always reached at the point where combustion begins; therefore, its position depends also on the morphology of the specimen. This will certainly produce larger standard deviations of the  $T_o$ , which is consistent with our observations (**Figure 2.9** inset).



**Figure 2.10:** Heating rate dependence of the residual mass,  $M_{res}$ , and its standard deviation,  $\sigma_{M_{res}}$  (inset).

TGA traces obtained at 100 °C/min heating rate (**Figure 2.8**) do not exhibit signs of combustion. Instead, mass loss occurs rather gradually in the (400 to 600) °C temperature range. Derivative mass loss curves do not have well-defined peaks and appear rather irreproducible, making it impossible to define  $T_o$ . As noted above, combustion increases with the specimen heating rate up to approximately 50 °C/min. So, in this case, the rate of the temperature increase in the TGA furnace is actually higher than the maximum heating rate of the specimen that can be achieved even with the help of combustion. This means that there has to be a significant time lag between furnace and specimen temperatures, and that mass loss rate depends mostly on the morphology of the particular sample. This explains the gradual mass loss and poor reproducibility of the derivative mass curves.

TGA results obtained with higher heating rates (allowing combustion) become increasingly less reliable, with standard deviations of  $T_o$  and  $M_{res}$  rapidly increasing (resulting in a systematic decrease in the  $M_{res}$  values). Therefore, it is important to collect TGA data with heating rates that do not allow combustion. For the particular specimen used in this study, only heating rates of (1 and 2.5) °C/min preclude combustion. However, we have noticed that purified samples that have much less active catalyst can be run at higher heating rates without combustion.



Selection of the heating rate is also of practical importance. Usually a sample has to be heated to at least 800 °C, which requires 13.3 h at a rate of 1 °C/min, compared to 8 min at 100 °C/min. Heating fast saves time, so the majority of researchers have used (10 – 20) °C/min rates. Based on the discussion above, we have selected 5 °C/min as a compromise, as each run takes less than 3 h and we avoid combustion for most types of samples.

#### 2.7.4 Sample Compaction

There is a huge difference in the morphology of “as-is” nanotube material and material that has been processed into buckypaper (usually after purification, but sometimes unpurified material is processed into buckypaper by dispersing in a solvent, filtering, and drying). The apparent density of unprocessed, “as-is” “fluffy” material can be (1 to 2) orders of magnitude smaller than that of processed material. It is difficult to place more than (2 to 4) mg of unprocessed material into the sample pan. As a result, some researchers have employed mechanical compaction as a means to increase apparent density and specimen size.

We have compared TGA results of “as-is” material with material compacted in a standard KBr die of 7 mm diameter by applying (0.5, 1.2 and 2.6) GPa pressure in a hydraulic press. The values of  $M_{\text{res}}$  were essentially unaffected, while compacting at progressively higher pressure leads to a (10 to 20) °C decrease in the  $T_0$  values. However, changes in  $T_0$  do not follow a uniform trend.  $T_0$  decreases from 417 °C to 395 °C as compacting pressure goes from (0 to 0.5) GPa and then increases to 403 °C as compacting pressure increases to 2.6 GPa. Compacting pressure does not affect the standard deviations of  $M_{\text{res}}$  and  $T_0$ . The reasons for this behavior are not clear. We have noticed that combustion still occurs at a heating rate of 5 °C/min, which is probably related to the presence of a considerable amount of active Fe catalyst particles.

We conclude that it is better to avoid compaction, as results are difficult to predict. Compaction may be necessary for some especially “fluffy” materials, but then results should be considered with full understanding that  $T_0$  may have been affected. In these cases, smaller compaction pressure is preferable. Generally, it is advisable not to compact the material by any means, which places the (2 to 4) mg limit on the sample size for unprocessed material. It may be preferable to use the same sample size for processed materials, as samples of dramatically different mass may behave differently. For example, a much larger sample may heat up slower due to its higher thermal capacity.

## References

1. Sivaram Arepalli, Pavel Nikolaev, Olga Gorelik, Victor Hadjiev, Williams Holmes, Bradley Files and Leonard Yowell, *Carbon* **42**, 1783 (2004).
2. “Applications Library on Thermal Analysis from TA Instruments”, <http://www.tainstruments.com/main.aspx?id=46&n=2&siteid=11>
3. “Application Notes on Thermal Analysis by Perkin Elmer”, <http://las.perkinelmer.com/search/Search.htm?Ntt=thermal+analysis&Ne=15&N=72+33+64+16&tab=NONE>
4. ASTM E1131 – Standard Test Method for Compositional Analysis by Thermogravimetry
5. W.E. Alvarez, B. Kitiyanan, A. Borgna, D.E. Resasco, *Carbon* **39**, 547 (2001).
6. A. G. Rinzler, J. Liu, H. Dai, P. Nikolaev, C. B. Huffman, F. J. Rodriguez-Macias, P. J. Boul, A. H. Lu, D. Heymann, D. T. Colbert, R. S. Lee, J. E. Fischer, A. M. Rao, P. C. Eklund and R. E. Smalley, *Appl. Phys. A* **67**, 29 (1998).
7. J. L. Bahr, J. P. Yang, D. V. Kosynkin, M. J. Bronikowski, R. E. Smalley and J. M. Tour, *J. Amer. Chem. Soc.* **123**, 6536 (2001).
8. Frank Hennrich, Ralf Wellmann, Sharali Malik, Sergei Lebedkin and Manfred M. Kappes, *Phys. Chem. Chem. Phys.*, **5**, 178 (2003).

### **3. Near-Infrared (NIR) Spectroscopy**

**Robert Haddon and Mikhail Itkis**  
**University of California, Riverside**

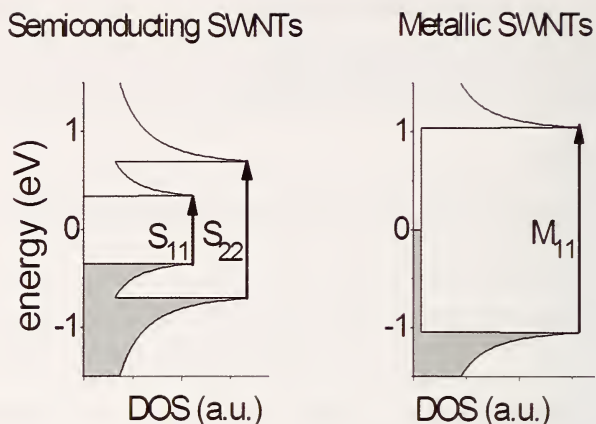
#### **3.1 Introduction**

Near-infrared (NIR) spectroscopy is an analytical technique which is ideally suited for the characterization of single-walled carbon nanotubes (SWNTs), because it allows the measurement of the absorption of light in the region of the interband electronic transitions. These electronic transitions are the characteristic signature of the SWNT electronic structure and may be observed in the solution or solid state as a function of photon energy. NIR transmission spectroscopy has been extensively used to detect SWNT interband transitions (1-8), to evaluate the effect of ionic and covalent chemistry on the band structure (7, 9-13), and to compare the abundance and diameter distribution of the SWNTs produced by different synthetic techniques as a function of synthetic parameters and catalyst composition (14-17).

Recently, NIR spectroscopy has been advanced as an efficient tool to quantitatively evaluate the carbonaceous purity of bulk SWNT material (18-22). The procedure is extremely simple, can be efficiently used by students and technical personnel and utilizes equipment that is routinely available in many research and educational laboratories. In this chapter we formulate the main principles of the NIR spectroscopy-based purity evaluation technique. We present examples of the practical use of this technique for optimization of SWNT synthesis and for improving the parameters of a purification procedure. We provide an assessment of the advantages and potential limitations of this purity evaluation technique against other carbon nanotube purity assessment methods.

#### **3.2. Formulation of method: Electronic Structure and Optical Spectroscopy of SWNTs**

The electronic structure of SWNT derives from that of a 2-D graphene sheet, but because of the radial confinement of the wave function the continuous electronic density of states (DOS) in graphite divides into a series of spikes in SWNTs which are referred to as Van Hove singularities (Figure 3.1) (23-26).



**Figure 3.1:** Electronic density of states (DOS ) of semiconducting and metallic SWNTs

Depending on helicity and diameter, these 1-D nanostructures may be metals or semiconductors(23-26).

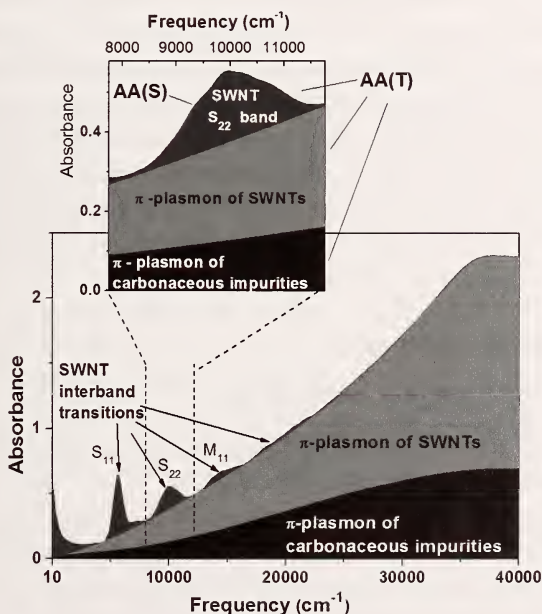
Based on simple tight-binding theory, the semiconducting SWNTs give rise to a series of electronic transitions between the principal mirror spikes in the electronic density of states (DOS) starting with  $S_{11} = 2a\beta/d$  and  $S_{22} = 4a\beta/d$ , while the metallic SWNTs show their first transition at  $M_{11} = 6a\beta/d$ , where  $a$  is carbon-carbon bond length (nm),  $\beta$  is the transfer integral between  $p\pi$ -orbitals ( $\beta \approx 2.9$  eV) and  $d$  is SWNT diameter (nm) (5, 23-26). Current synthetic techniques produce SWNTs with a range of chiralities and diameters, and in this case the  $S_{11}$ ,  $S_{22}$  and  $M_{11}$  features are simultaneously present in the electronic spectra of the bulk SWNT sample with individual features broadened due to the finite SWNT diameter distribution (2, 3, 5, 7, 8). NIR optical absorption spectroscopy can capture these specific features which typically occur between (0.5 and 3) eV (2, 3, 5, 7, 8). The optical spectra of carbonaceous and graphitic impurities present in bulk SWNT samples give rise to a featureless monotonically increasing absorption in this spectral region (0.5 to 4) eV (18-20, 27, 28). These spectral characteristics provide a unique opportunity to distinguish between the SWNTs and impurities present in the sample using optical spectroscopy.

Figure 3.2 shows a schematic of the absorption spectrum of a typical electric arc discharge (EA) produced SWNT sample in the spectral range between the far-IR and the ultra-violet (UV) ( $10$  to  $45\,000\text{ cm}^{-1}$ ), with the absorptions due to SWNTs and carbonaceous impurities shown in different colors to illustrate the different components (although it is not yet possible to analytically separate these contributions) (19, 20). The high-energy part of the spectrum is dominat-



ed by the  $\pi$ -plasmon absorption from both SWNTs and carbonaceous impurities, and the tail of this peak extends into the far-IR part of the spectrum. The NIR - visible part of the spectrum from (4000 to 17 000)  $\text{cm}^{-1}$  exhibits characteristic absorption features, originating from the interband transitions between pairs of Van Hove singularities in semiconducting and metallic SWNTs, which ride on the top of the  $\pi$ -plasmon tail. It is intuitively understandable, that the strength of these characteristic features in comparison with the featureless baseline provides a measure of the purity of the SWNT material.

While the  $S_{11}$  transition is the most prominent, we chose the second semiconducting transition ( $S_{22}$ , inset to Figure 3.3), for the purity evaluation because the  $S_{22}$  transition is less susceptible to incidental doping and because it matches the



**Figure 3.2:** Schematic illustration of the optical spectrum of typical SWNT sample produced by the electric arc method. Inset shows the region of the  $S_{22}$  interband transition utilized for NIR purity evaluation. In the diagram: AA(S) is the area of  $S_{22}$  spectral band after linear baseline correction; AA(T) is the total area of the  $S_{22}$  band including SWNT and carbonaceous impurity contributions. The NIR relative purity is given by  $RP = (AA(S)/AA(T))/0.141$  (see text).

transmission window for dimethylformamide (DMF) which is utilized for the solution (dispersion) phase NIR spectroscopy (18-20). It is known that DMF is one of the most efficient solvents for dispersing both raw and purified SWNT material, and we have found that DMF can partially compensate the incidental doping affecting the  $S_{22}$  interband transition (18-20).

We have identified the ratio  $AA(S)/AA(T)$  as the simplest possible metric of SWNT purity, where  $AA(S)$  is the area of the  $S_{22}$  interband transition after linear baseline subtraction (dark gray area in the inset to Figure 3.2), and  $AA(T)$  is the total area under the spectral curve, with both areas taken between the spectral cutoffs of (7750 and 11750)  $\text{cm}^{-1}$ , which were chosen to capture the  $S_{22}$  interband electronic transitions of SWNTs of the diameter produced by the EA-process with Ni/Y catalysts (18-20). This ratio is then normalized by dividing by 0.141, the value of  $AA(S)/AA(T)$  obtained for an arbitrary high purity reference sample of AP-SWNTs (denoted R2), and this procedure therefore gives rise to a relative purity (RP) (18-20). Because a 100 % pure reference sample is not currently available, it is not possible to give an absolute determination of SWNT purity, although progress may be noted (27, 28). Nevertheless, through the joint efforts of the carbon nanotube community, and with sample exchanges between research groups it will be possible to further refine the choice of a reference sample and to asymptotically converge on a standard for the measurement of absolute purity.

### 3.3 Practical Procedure

#### 3.3.1 Choice of Spectrophotometer

Common FT-IR spectrometers cover the spectral range between (10 000 and 400)  $\text{cm}^{-1}$ , i.e. (1000 to 25 000) nm, whereas UV-Vis (Visible) spectrophotometers usually cover the range between (175 and 900) nm, i.e., (57 000 to 11 000)  $\text{cm}^{-1}$ . In order to cover the typical  $S_{22}$  and  $M_{11}$  interband transitions which are of interest in the purity evaluation of SWNTs produced by electric arc and laser ablation techniques, a spectral range of (7000 to 19 000)  $\text{cm}^{-1}$  is required, so neither of these types of spectrophotometers encompass the required spectral range. Several commercial instruments combine the UV-Visible and NIR spectral ranges and are suitable for the NIR purity evaluation procedure.

#### 3.3.2 Sample preparation

For accurate evaluation of bulk quantities of SWNT material (>10 g), special attention must be paid to the preparation of the NIR samples, because as-prepared SWNT (AP-SWNT) material is typically very inhomogeneous. Below we present a multi-step best practices procedure developed for large scale batches of inhomogeneous AP-SWNT material (18-20):

**Step 1.** The AP-SWNT material is mechanically homogenized to give a dry powder. The use of a kitchen blender operated at low speed for 5 min leads to a fine homogeneous powder.

**Step 2.** Homogenized AP-SWNT soot (50 mg) is dispersed in 100 mL of DMF by use of an Aquasonic 50T, 75T, or 550T ultrasonic bath or equivalent brand for (10 to 20) min. Mechanical stirring facilitates homogenization during this step which should lead to a homogeneous concentrated slurry of SWNTs in DMF.

**Step 3.** A few drops of the concentrated SWNT slurry is collected by pipette from different regions of the sample and diluted to 10 mL with fresh DMF and sonicated for 10 min. By use of one or two additional 10 mL scale dilution-ultrasonication cycles the concentration is reduced to  $\approx 0.01$  mg/mL, which provides a stable, visually non-scattering dispersion with an optical density close to 0.2 at  $12,000\text{ cm}^{-1}$  in a 10 mm path-length cell.

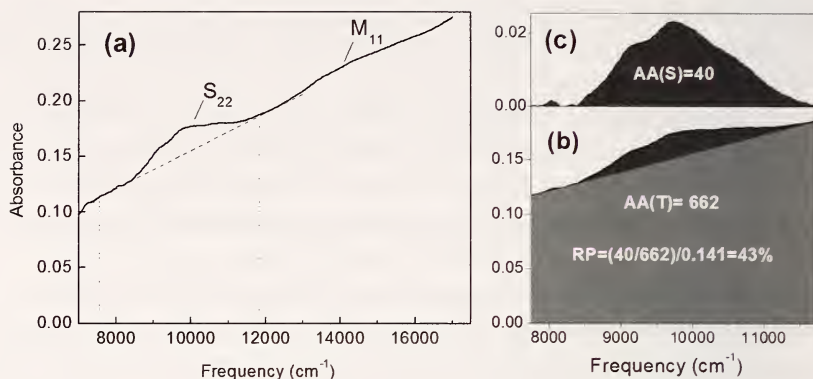
This preparation procedure results in a test sample, which provides a reproducible and accurate representation of the carbonaceous purity of bulk AP-SWNT soot. Increasing the SWNT concentration in the final test sample improves the signal-to-noise ratio of the experimental optical spectrum, but may destabilize the dispersion and lead to significant light scattering and thereby compromise the results of the purity evaluation.

For purified SWNT samples the amount of material utilized for the purity evaluation test can be reduced to a few mg because the material is usually fairly well homogenized and less material is required to give a statistically representative sample. In order to assure homogenization we recommend the use of a standard coffee blender to convert purified SWNT material into a fine powder.

### 3.3.3 Practical example of spectral measurements and relative purity calculations

The SWNT sample should be ultrasonicated just before the spectral measurement in order to assure high quality dispersion, and the spectrometer should be turned on 30 min prior to the measurement to allow the baseline to stabilize. Spectra are usually taken in the range ( $7000$  to  $17\,000$ )  $\text{cm}^{-1}$  for EA-produced SWNTs in order to visualize both the  $S_{22}$  and  $M_{11}$  interband transitions. Some spectrophotometers allow the collection of spectra only as a function of wavelength. For purity calculations we recommend processing the data as a function of frequency (energy) as shown in Figure 3.3, because the absorbance spectra as a function of wavelength (proportional to inverse energy) show significantly more curvature and are more difficult to analyze.



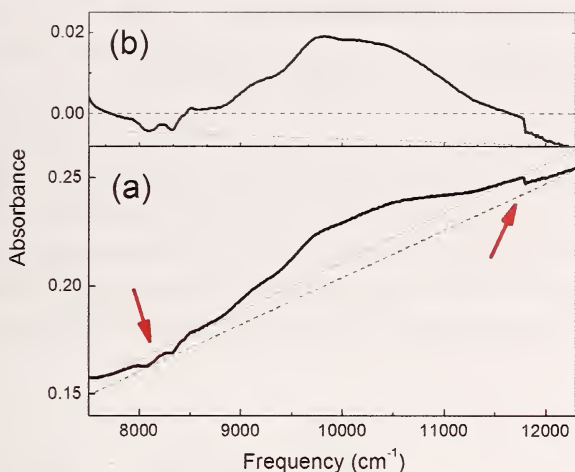


**Figure 3.3:** Practical procedure for determination of relative purity (RP) of AP-SWNT sample: a) Solid line: spectrum of SWNT dispersion in DMF in the range (7000-17 000) cm<sup>-1</sup>, dashed line: linear baseline, dotted lines: spectral cutoffs for purity determination; b) Total area AA(T) (black + gray) in the region of the S<sub>22</sub> interband transition, calculated integral AA(T)=662; c) Area of S<sub>22</sub> feature AA(S) (gray) after linear baseline correction, integral AA(S)=40. RP = 43 %

In order to establish the baseline a tangent line is drawn to the minima of the absorption curve at the low and high energy sides of the S<sub>22</sub> transition (Figure 3.3a); in practice it is best to use 5 data-points on each side of the chosen S<sub>22</sub> spectral window (7750 to 11750 cm<sup>-1</sup> for EA -SWNTs) for the linear fitting routine. The absorption spectrum within the cutoffs is presented separately in Figure 3.3b with calculated total area AA(T) = 662. Figure 3.3c shows the spectrum of the S<sub>22</sub> feature after linear baseline correction with integrated area AA(S)=40. The ratio AA(S)/AA(T) is divided by 0.141 to obtain a relative purity, RP against the P2 reference sample:(18-20) in the present case RP = 43 % (Figure 3.3).

### 3.3.4 Most common source of experimental uncertainty: distorted baseline

Figure 3.4 presents a NIR spectrum of a SWNT dispersion in DMF exhibiting both of the two most common spectral distortions which occur in the vicinity of (8000 and 12 000) cm<sup>-1</sup> (red arrows). The distortion just above 8000 cm<sup>-1</sup> is due to presence of traces of water in the solvent which gives very strong absorptions that in some cases can not be properly subtracted from the baseline by the pure solvent in the reference channel.



**Figure 3.4:** Example of distortions in NIR spectra (red arrows) due to the presence of traces of water in the DMF and the change of optical elements in the spectrophotometer. (a) complete spectrum, (b) spectrum of  $S_{22}$  feature after linear baseline correction. Choice of baseline is uncertain (between blue and green dashed lines), which leads to uncertainties in the integrated areas AA(T) and AA(S) and in the calculated value of the relative purity.

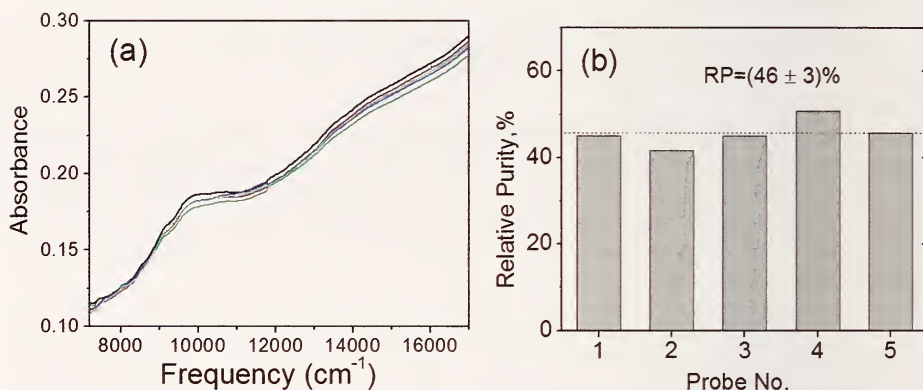
In the example given in Figure 3.4 this distortion produces a negative contribution to the integrated area thus reducing the relative purity because of the uncertainty in the baseline position at the low energy spectral cutoff. It is important to use dry solvent and to avoid admitting any traces of water to the solvent during the sample preparation procedure.

The step in the trace in the vicinity of 12 000  $\text{cm}^{-1}$  corresponds to the change from the NIR detector to the UV-Vis detector in the spectrophotometer and introduces uncertainties into spectrum and the linear baseline correction near the high-energy spectral cutoff. Possible baseline choices are shown by green and blue colors and this uncertainty serves to introduce uncertainties into the calculated RP. The jumps in the spectrum result from the change of the optical elements inside the spectrophotometer and can be minimized by careful alignment of spectrophotometer components by the manufacturer, optimum alignment of the sample positions in both optical channels, by modifying the ratio of spectral resolutions in the NIR and UV-Vis spectral ranges, and by stabilization of the spectrometer by utilizing an extended warm-up time. It is practically impossible to avoid such steps in the case of scattering samples such as poorly dispersed SWNTs or inhomogeneous or thick SWNT films.

### 3.4 Characterization of NIR method

#### 3.4.1 Reproducibility of the purity evaluation

To test the reliability of the NIR technique and the reproducibility of the purity measurements we prepared five independent 50 mg probe samples from the same mechanically homogenized 10 g batch of AP-SWNT material using the recommended procedure.(18-20) The results of the NIR relative purity measurements are presented in the Figure 3.5. The five probe samples show an average relative purity of 46 % with a standard deviation of 3.0 %, which corresponds to relative uncertainty  $\sim 7\%$  in the measured RP value.

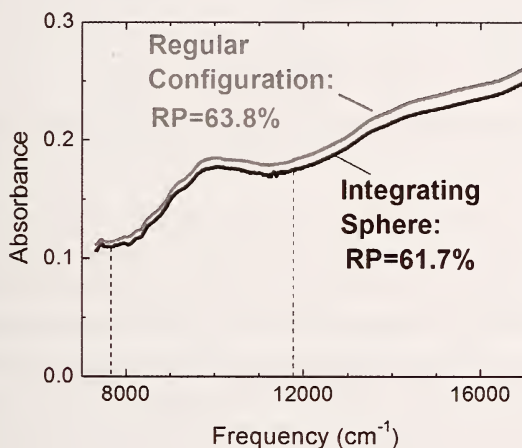


**Figure 3.5:** Reproducibility test of NIR purity evaluation technique: a) Solution phase NIR spectra of five independent probe samples obtained from 10 g AP-SWNT sample; b) Calculated purity of the five probe samples

#### 3.4.2 Influence of light scattering

The NIR purity evaluation method depends on the absorption of light, but the interaction of electromagnetic radiation with SWNTs may lead to scattering(19, 20, 29). The occurrence of light scattering would be a complicating factor in the interpretation of the absorption spectra of SWNTs and might affect the accuracy of the purity evaluation by contributing to the level of the baseline (Figure 3.3), thus reducing the measured purity. The spectral contribution to light scattering (S) is controlled by the ratio of the characteristic dimension of the scattering particles (d) and the wavelength of the incident light ( $\lambda$ ). In the present situation, we consider the SWNT length to be the characteristic dimension d, because the strongest interaction of light with SWNTs occurs when the

light is polarized along the SWNT axis. Most SWNT samples show a wide length distribution, which is typically concentrated in the range  $d = (0.5 \text{ to } 3) \mu\text{m}$  and this is comparable with the wavelength of light in vicinity of the  $S_{22}$  interband transition ( $\lambda \approx 1 \mu\text{m}$ ) that is utilized for purity evaluation. In this circumstance ( $d \approx \lambda$ ) Mie scattering is expected to dominate,(19) and this scattering mechanism becomes more important as the particle size increases ( $d > \lambda$ ). In the spectral range of interest there is a crossover between  $\lambda > d$  and  $\lambda < d$ , and this makes it difficult to theoretically estimate the influence of scattering on the NIR absorption spectra, especially in the case of SWNT solution samples which present themselves to the light beam as dynamic highly anisotropic particles.



**Figure 3.6:** Solution phase absorption spectra of a SWNT sample collected with the spectrophotometer in regular transmission configuration (gray curve) and using an integrating sphere (black curve) to collect the scattered light.

In order to experimentally address these questions, we made use of an integrating sphere in the sample compartment of the Cary 500 UV-Vis-NIR spectrophotometer utilized in our experiments,(20) as discussed previously (29). The integrating sphere recovers a significant fraction of the scattered light normally lost with the narrow aperture of collection presented in a standard transmission experiment. Figure 3.6 shows the NIR absorption spectra of an AP-SWNT dispersion in DMF measured with regular and integrating sphere configurations for the collection of light (20). The introduction of the integrating sphere collection leads to a small decrease in the level of the baseline, and the calculated



relative purities were found to be  $RP = 63.8\%$  in regular, and  $RP = 61.7\%$  in the integrating sphere configurations; Table 1 shows a comparison for three AP-SWNT samples with relative purities between 20 and 60 % (20). If scattering were to be significant, we would expect a reduction in the relative purity, when measured in the regular configuration in comparison with the case of the integrating sphere technique. Table 1 shows the opposite trend, with a lower measured relative purity in the integrating sphere configuration, although the deviations are within the experimental accuracy of our technique (18-20). This

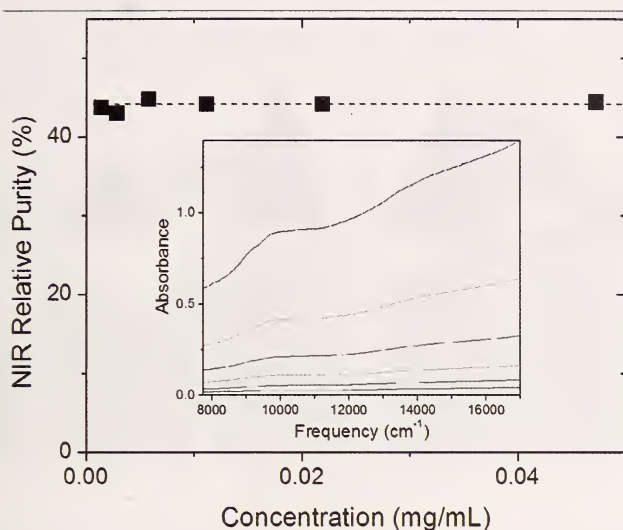
**Table 1. Measured NIR Purity with Spectrophotometer in Regular and Integrating Sphere Configuration**

Sample Number	1	2	3
Regular Configuration	20.5 %	38.5 %	63.8 %
Integrating Sphere	16.5 %	35.5 %	61.7 %

suggests, that in the case of properly dispersed SWNTs, scattering does not materially affect the NIR relative purity evaluation. Incompletely dispersed samples with large aggregates of SWNTs would be expected to affect the purity evaluation as a result of Mie scattering, and it was for this reason that we emphasized the importance of the sample preparation procedure and stressed the necessity of utilizing low SWNT solution concentrations ( $\leq 0.01$  mg/mL) (18-20). It proved to be more difficult to control scattering in the case of SWNT thin films, and this was one factor which lead to our choice of solution phase (18-22) rather than thin film (7, 14, 15, 17) transmission spectroscopy for the relative purity evaluation studies.

### 3.4.3 Influence SWNT concentration on relative purity determination

We previously recommended a concentration of 0.01 mg/mL for the SWNT purity evaluation;(18) higher SWNT concentrations are difficult to stabilize as non-scattering dispersions, while reducing the concentration decreases the signal to noise ratio of the NIR spectra. In order to evaluate the importance of the SWNT concentration for NIR spectroscopy-based purity evaluation technique we prepared a series of dispersions of AP-SWNTs with concentrations between 0.05 and 0.001 mg/mL.(20) Figure 3.7 shows the NIR relative purities obtained from the NIR spectra shown in the inset, as a function of SWNT concentration.



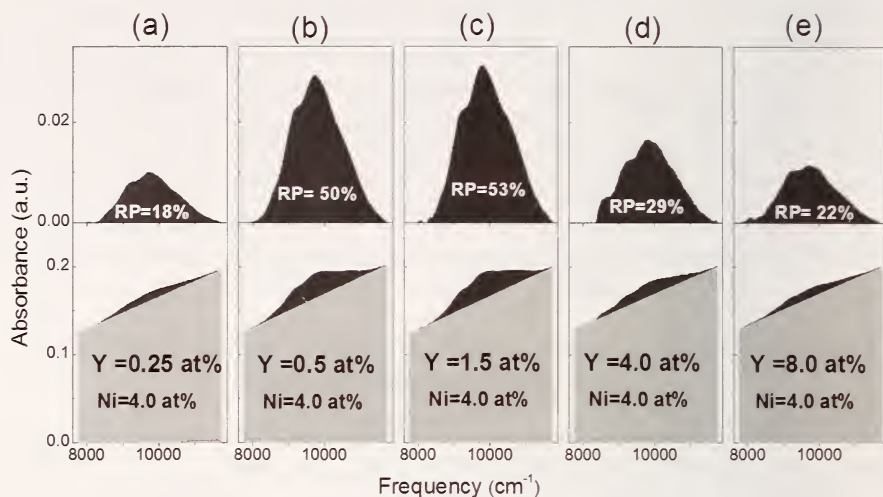
**Figure 3.7:** NIR relative purity as a function of the concentration of the SWNT dispersion; inset shows experimental NIR solution phase spectra utilized for calculation of purity.

Figure 3.7 demonstrates that the NIR relative purity values are independent of the SWNT concentrations, which is a simple consequence of the applicability of Beers law to SWNT dispersions (27, 28). This confirms that the relative purities determined by the NIR technique are internally consistent, and that the sample preparation procedure does not require exact matching of the concentrations.

### 3.5 Examples of the application of NIR purity evaluation procedure

#### 3.5.1 Optimization of SWNT synthesis

Figure 3.8 illustrates the use of the NIR-based purity evaluation technique for the study of the effect of the Y concentration on the large scale Ni/Y catalyzed EA-discharge Ni/Y production of SWNTs.(16) The bottom panels in Figure 3.8(a-e) show the region of the solution phase NIR spectra in the range of (7750 to 11750)  $\text{cm}^{-1}$  corresponding to the  $S_{22}$  interband transition for five Y concentrations between (0.25 and 8) atom % .



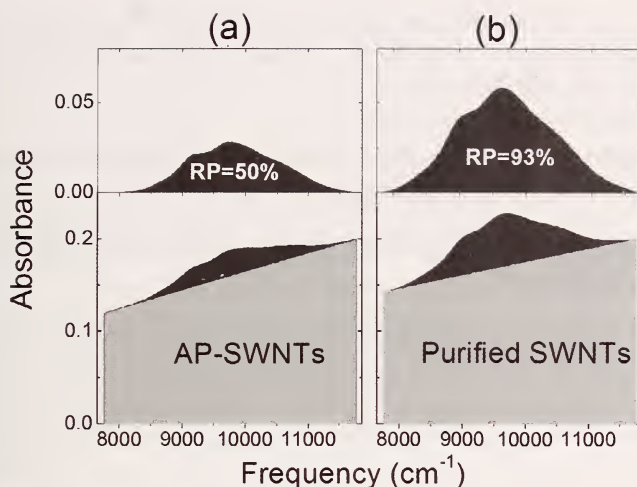
**Figure 3.8:** Solution phase NIR spectra of EA-AP-SWNT soot produced with Ni-Y binary catalyst as a function of the Y concentration at a constant Ni concentration of 4 atom %. Bottom panel: spectra in the range of S22 interband transition consisting of featureless background (gray area) and S22 SWNT feature (black area) separated by the linear baseline; Top panel: the enlarged S22 interband transition obtained after the linear baseline subtraction. The relative carbonaceous purity of the AP-SWNT soot (top panel) is determined from the ratio of the area under the spectral curve in the top panel to the total spectral area in the bottom panel.

The top panels in Figures 3.8(a-e) show the corresponding S22 features extracted from the original spectra (bottom panel) by a linear baseline correction. High purity SWNT samples have a high ratio of the area of the S22 band (top panel) to the total area under the spectral curve (bottom panel). It is clear from Figure 3.8 that the highest ratio and therefore the highest purity occurs in the vicinity of Y concentrations of (0.5 and 1.5) atom % in agreement with prior work (30). Thus, the NIR technique provides an efficient tool to visualize and analytically evaluate the effect of catalyst composition and other synthesis parameters on the purity of the AP-SWNT product (16, 21).

### 3.5.2 Evaluation of efficiency of purification and optimization of purification parameters

An important application of a purity evaluation technique is the ability to efficiently monitor and optimize the parameters of purification processes.(31-33) Figure 3.9 shows the NIR spectra of the starting AP-SWNT material and the final purified product obtained by oxidation of AP-SWNTs in air followed by treatment with hydrochloric acid. According to the NIR evaluation procedure





**Figure 3.9:** NIR evaluation of efficiency of purification procedure. NIR spectra in the range of the SWNT S22 interband transition for: (a) starting (AP) sample (NIR RP=50 %), (b) purified (NIR RP=93 %) sample; bottom panel – full spectra, top panel - S22 band after linear baseline subtraction.

the carbonaceous relative purity increased from (50 to 93) % as a result of the purification (Figure 3.9) and the amount of residual metal catalyst decreased from (30 to 8) %, as determined by TGA.

It is convenient to introduce the purification recovery factor PRF (31, 33), which takes into account both the increase of purity and the loss of product; for an ideal process the product is analytically pure and  $PRF = 1$  (33). If  $Y$  is the yield of the process then we have shown that the PRF is given by (33):  $PRF = [RP(P-SWNT)/RP(AP-SWNT)] \times Y$ , where  $RP(P-SWNT)$  and  $RP(AP-SWNT)$  are the relative purities of the as-prepared and purified SWNTs. Because the NIR technique applies to the carbonaceous purity of the sample the measured yield must be corrected for changes in the metal content of the sample and in this case the yield is given by  $Y = [M_{fin} \times (1-MET_{fin})]/[M_{st} \times (1-MET_{st})]$ , where  $M_{st}$  ( $M_{fin}$ ) and  $MET_{st}$  ( $MET_{fin}$ ) are the sample mass and the fraction of metal, respectively, in the starting material (final product). For example, in the purification procedure of AP-SWNTs illustrated in Figure 3.9,  $M_{st}=10$  g,  $RP(AP-SWNT) = 50$  % and  $MET_{st} = 0.3$  (metal residue of 30 % determined by TGA); after purification  $M_{fin} = 2.5$  g,  $RP(P-SWNT) = 93$  % and  $MET_{fin} = 0.092$ ; leading to  $PRF = 0.61$  for the process. Thus about 40 % of the SWNTs present in the starting sample were lost during the purification process. Each step of a

purification procedure can be evaluated and optimized on the basis of NIR relative purity and PRF figure of merit (31-33) taking into account that the ideal purification process results in a  $PRF = 1$ .

### **3.6 Frequently asked questions about the capabilities and limitations of the NIR technique:**

**The NIR technique provides a value for the relative purity (RP) - what about the absolute purity?**

At the present moment it is not possible to provide an absolute value of the purity of SWNTs, but it is expected that the widespread adoption of the NIR purity evaluation technique supported by other analytical techniques presented in this guide will soon produce samples which cannot be further purified and may thus be considered analytically pure. The joint efforts of the carbon nanotube community, and sample exchanges between research groups will be required to asymptotically converge on a standard for the measurement of absolute purity. Based on currently available samples, we expect analytically pure SWNT samples to be characterized by values of  $AA(S)/AA(T) \approx 0.325$  and  $RP \approx 230\%$  when evaluated against the original reference sample R2.(20, 28)

**To which types of SWNTs is the NIR purity evaluation technique applicable?**

The NIR purity evaluation technique was initially developed for electric arc produced SWNTs prepared with the Ni/Y catalyst, but it has already been successfully adapted to SWNTs produced by laser ablation (34). For the applicability of NIR technique it is important that the SWNTs have a relatively narrow diameter distribution without overlap between the  $S_{11}$ ,  $S_{22}$  and  $M_{11}$  bands (28).

**Is the NIR technique applicable to CVD produced SWNTs?**

The chemical vapor deposition (CVD) technique usually produces SWNTs with an extremely wide diameter distribution. As a result, there is significant overlap of the interband transitions in these preparations, and this obscures the NIR spectral features and severely complicates the application of the current procedure. Recently, much higher selectivity of SWNT diameters and chiralities was achieved by modifying the catalyst preparations used in the CVD technique (35) and by the application of separation procedures (36), and the technique is applicable to such samples.

## Is NIR technique applicable to HiPco produced SWNT?

The SWNT diameter distribution of HiPco SWNTs is wider than that of SWNTs produced by the electric arc and laser ablation techniques, but narrower than that of most CVD-produced SWNTs. In the optical spectra of HiPco material, the  $S_{11}$ ,  $S_{22}$  and  $M_{11}$  bands are partially overlapping, so the direct calculation of the  $AA(S)/AA(T)$  ratio results in an underestimated relative purity. Nevertheless, the utilization of the NIR technique can be very useful for the comparison of SWNT content from batch-to-batch for both manufacturers and end-users of HiPco SWNTs, so an internal HiPco reference standard should be developed. Currently, there is no algorithm available to compare the purity of the best laser produced material against the best HiPco produced sample, so the development of absolute purity standards for each production technique is very important (28).

## Why is the linear baseline approximation used in the NIR purity evaluation procedure when a non-linear baseline fit might be more accurate?

We utilized the linear baseline approximation, because it provides a simple, easily applicable and consistent purity evaluation procedure without any fitting parameters. More sophisticated non-linear baseline descriptions have been advanced (21, 22); however, these techniques require multiple fitting parameters for the purity evaluation procedure. Near-IR absorption studies of a number of different forms of carbon, including the products of EA synthesis and commercially available carbon-based nanomaterials(27, 28), has shown that the shape of the baseline in the range of the  $S_{22}$  interband transition depends critically on the type of nanocarbon, and this compromises the transferability of the parameters from non-linear baseline fitting procedures.

## The NIR purity evaluation procedure implicitly assumes that the extinction coefficients of the SWNTs and carbonaceous impurities are equal on a per carbon basis. How does this affect the results of purity evaluation?

The ultimate goal of this work is the establishment of the absolute extinction coefficients which would remove this objection and allow measurement of the absolute purity of the samples (27, 28). The simple metric of purity adopted herein [ $AA(S)/AA(T)$ ] assumes that the per carbon extinction coefficients of SWNTs and carbonaceous impurities are identical. If the extinction coefficient of the impurities is higher than that of the SWNTs, the  $AA(S)/AA(T)$  ratio would underestimate the purity, whereas the purity would be overestimated in the opposite case. Current research suggests that the extinction coefficient of SWNTs produced in the electric arc is higher than that of the carbonaceous impurities (27, 28).

**The NIR technique utilizes the semiconducting  $S_{22}$  interband transition for purity evaluation. What can be said about the metallic SWNTs?**

The majority of known bulk synthetic techniques produce a statistical mixture of SWNTs, which corresponds to a 2:1 ratio between semiconducting and metallic SWNTs (16), although certain CVD techniques are chirality selective(35). Thus we assume the semiconducting  $S_{22}$  interband transition provides a measure of the purity of the whole SWNT sample.

**Is it possible to use other solvents instead of DMF?**

DMF is a good solvent for the purity evaluation technique, because it is one of the best solvents for dispersing SWNTs, does not absorb NIR radiation in the range of the  $S_{22}$  band and reduces the incidental doping effect of the SWNTs. Other solvents are applicable for purity evaluation, but the AA(S)/AA(T) ratio varies among solvents. For example, we found that the AA(S)/AA(T) ratio in water is lower than in DMF not only for purified (doped) material, but also for AP-SWNTs. Thus we recommend the use of a single solvent (even if not DMF) for the purity evaluation routine within a particular set of experiments.

**Is it possible to use thin film instead of solution phase spectroscopy?**

Thin film spectroscopy has been extensively used in SWNT research. Some types of SWNTs are very difficult to disperse, especially long SWNTs or purified SWNTs after high temperature annealing in vacuum. In this case some users of the NIR technique prefer to spray a thin film of SWNTs on an optical substrate for use in NIR spectroscopy. This approach is entirely legitimate (14, 37), but we found it more difficult to obtain reproducible AA(S)/AA(T) ratios, that the results were somewhat dependent on the thickness of the film and that it is not trivial to obtain homogeneous non-scattering films (29), as opposed to non-scattering dispersions (20). Similar to the case of different solvents, the ratio AA(S)/AA(T) can be different for a sample in the solution phase and as a thin film, so it is important to be consistent in the use of either solution phase or thin film spectroscopy during a set of experiments.

**How does debundling (rebundling) of SWNTs affect the results of the purity evaluation?**

It has been shown that debundling of the SWNTs or the separation of individual SWNTs leads to better resolved absorption spectra with narrow peaks corresponding to the interband transitions of SWNTs of particular chirality (38). Does such debundling affect the AA(S)/AA(T) ratio? To a first approximation we do not expect that debundling and the resultant change of the



shape of the spectra would affect the integral values AA(S) and AA(T) and the measured purity value. However, at the present time, there are no experimental data comparing optical spectra of the same ensemble of SWNTs in individual and bundled forms, so this point remains uncertain.

### **How does the interpretation of the absorption features affect the results of the purity evaluation: Interband transitions versus excitons**

In the past few years it has been proposed, that the observed S11, S22 and M11 bands do not correspond to interband transitions between pairs of Van Hove singularities, but are rather exciton bands due to the strong coupling of electrons and holes in the 1D-system (39, 40). This issue is not finalized yet, but there are no obvious reasons to suggest that a change of interpretation of the SWNT absorption feature would preclude utilization of this optical transition for purity evaluation purposes.

**Acknowledgement.** This work was supported by DOD/DARPA/DMEA under Awards No. DMEA90-02-2-0216 and H94003-04-2-0404.

### **References**

1. Chen J, Hamon MA, Hu H, Chen Y, Rao AM, et al. 1998. *Science* 282: 95-8
2. Kataura H, Kumazawa Y, Maniwa Y, Umezue I, Suzuki S, et al. 1999. *Synth. Met.* 103: 2555-8
3. Petit P, Mathis C, Journet C, Bernier P. 1999. *Chem. Phys. Lett.* 305: 370-4
4. Chen J, Rao AM, Lyuksyutov S, Itkis ME, Hamon MA, et al. 2001. *J. Phys. Chem. B* 105: 2525-8
5. Hamon MA, Itkis ME, Niyogi S, Alvaraez T, Kuper C, et al. 2001. *J. Am. Chem. Soc.* 123: 11292-3
6. Niyogi S, Hamon MA, Hu H, Zhao B, Bhowmik P, et al. 2002. *Acc. Chem. Res.* 35: 1105-13
7. Itkis ME, Niyogi S, Meng M, Hamon M, Hu H, Haddon RC. 2002. *Nano-Lett.* 2: 155-9
8. Hennrich F, Lebedkin S, Malik S, Tracy J, Barczewski M, et al. 2002. *Phys. Chem. Chem. Phys.* 4: 2273-7
9. Kazaoui S, Minami N, Jacquemin R, Kataura H, Achiba Y. 1999. *Phys. Rev. B* 60: 13339-42
10. Kazaoui S, Minami N, Matsuda N, Kataura H, Achiba Y. 2001. *App. Phys. Lett.* 78: 3433-5
11. Hennrich F, Wellmann R, Malik S, Lebedkin S, Kappes MM. 2003. *Phys. Chem. Chem. Phys.* 5: 178-83



12. Kamaras K, Itkis ME, Hu H, Zhao B, Haddon RC. 2003. *Science* 301: 1501
13. Hu H, Zhao B, Hamon MA, Kamaras K, Itkis ME, Haddon RC. 2003. *J. Am. Chem. Soc.* 125: 14893-900
14. Jost O, Gorbunov AA, Pompe W, Pichler T, Friedlein R, et al. 1999. *App. Phys. Lett.* 75: 2217-9
15. Jost O, Gorbunov AA, Moller J, Pompe W, Lui X, et al. 2002. *J. Phys. Chem. B* 106: 2875-83
16. Itkis ME, Perea D, Niyogi S, Love J, Tang J, et al. 2004. *J. Phys. Chem. B* 108: 12770-5
17. Jost O, Gorbunov AA, Liu X, Pompe W, Fink J. 2004. *J. Nanosci. Nanotech.* 4: 433-40
18. Itkis ME, Perea D, Niyogi S, Rickard S, Hamon M, et al. 2003. *Nano Lett.* 3: 309-14
19. Haddon RC, Sippel J, Rinzler AG, Papadimitrakopoulos F. 2004. *MRS Bulletin* 29: 252-9
20. Itkis ME, Perea D, Jung R, Niyogi S, Haddon RC. 2005. *J. Am. Chem. Soc.* 127: 3439-48
21. Krestinin AV, Kislov MB, Ryabenko AG. 2004. *J. Nanosci. Nanotech.* 4: 390-7
22. Ryabenko AG, Dorofeeva TV, Zvereva GI. 2004. *Carbon* 42: 1523-35
23. Saito R, Fujita M, Dresselhaus G, Dresselhaus MS. 1992. *Phys. Rev. B* 46: 1804-11
24. Mintmire JW, Dunlap BI, White CT. 1992. *Phys. Rev. Lett.* 68: 631-4
25. Hamada N, Sawada SI, Oshiyama A. 1992. *Phys. Rev. Lett.* 68: 1579-81
26. Dresselhaus MS, Dresselhaus G, Eklund PC. 1996. *Science of Fullerenes and Carbon Nanotubes*. San Diego: Academic
27. Zhao B, Itkis ME, Niyogi S, Hu H, Zhang J, Haddon RC. 2004. *J. Phys. Chem. B* 108: 8136-41
28. Zhao B, Itkis ME, Niyogi S, Hu H, Perea D, Haddon RC. 2004. *J. Nanosci. Nanotech.* 4: 995-1004
29. Lebedkin S, Hennrich F, Skipa T, Kappes M. 2003. *J. Phys. Chem. B* 107: 1949-56
30. Journet C, Maser WK, Bernier P, Loiseau A, Lamy de la Chappelle M, et al. 1997. *Nature* 388: 756-8
31. Sen R, Rickard SM, Itkis ME, Haddon RC. 2004. *Near-IR Spectroscopy as a Tool to Monitor the Purification of Single-Walled Carbon Nanotube Films by Thermal Oxidation*. Presented at Proceedings of the NATO Advanced Study Institute on Organic Conductors, Superconductors and Magnets: From Synthesis to Molecular Electronics, Corfu, Greece
32. Hu H, Zhao B, Itkis ME, Haddon RC. 2003. *J. Phys. Chem. B* 107: 13838-42

33. Hu H, Yu A, Kim E, Zhao B, Itkis ME, et al. 2005. *J. Phys. Chem. B* 109: 11520-4
34. Kim Y, Luzzi DE. 2005. *J. Phys. Chem. B* ASAP
35. Resasco DE, Herrera JE, Balzano L. 2004. *J. Nanosci. Nanotech.* 4: 398-407
36. Zheng M, Jagota A, Strano MS, Santos AP, Barone P, et al. 2003. *Science* 302: 1545-8
37. Sen R, Rickard SM, Itkis ME, Haddon RC. 2003. *Chem. Mater.* 15: 4273-9
38. O'Connell MJ, Bachilo SM, Huffman CB, Moore VC, Strano MS, et al. 2002. *Science* 297: 593-6
39. Ando T. 1997. *J. Phys. Soc. Japan* 66: 1066-73
40. Spataru CD, Ismail-Beigi S, Benedict LX, Louie SG. 2004. *Phys. Rev. Lett.* 92: 077402

## 4. Raman Spectroscopy

**Anna Swan, Boston University**

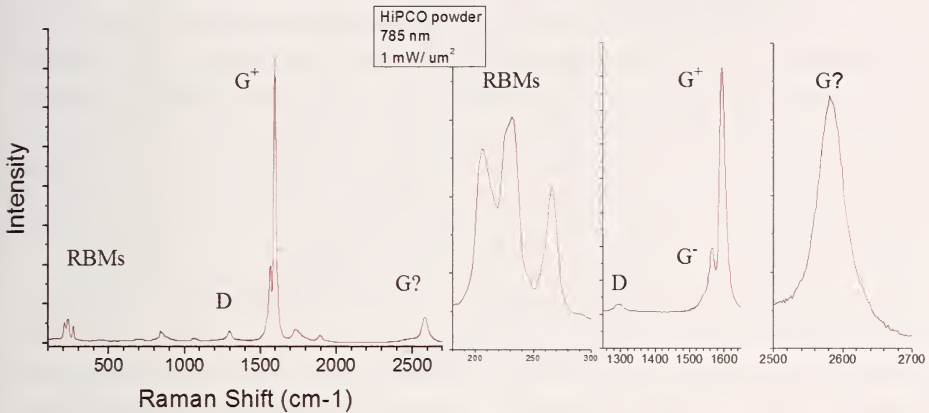
Raman spectroscopy is a widely used tool to characterize material composition, sample temperature, and strain from analysis of the material-specific phonon mode energies (1, 2). It requires very little sample preparation and a rapid, non-destructive optical spectrum is easily achieved.

Raman scattering is a weak interaction, and typically less than one in a million of the incoming photons exchanges energy with the phonons in bulk materials. The incoming light interacts with an electron that makes a virtual or real transition to a higher energy, where the electron interacts with a phonon (via electron-phonon coupling) before making a transition back to the electronic ground state. In this instantaneous process, energy and momenta are conserved so that  $E_{\text{scattered}} = E_{\text{laser}} \pm h\Omega$  for Stokes (-) and Anti-Stokes (+) scattering respectively, with  $\Omega$  being the frequency of the particular phonon mode. The energy of the inelastically scattered light is measured with respect to the laser energy (in  $\text{cm}^{-1}$ ), and by convention, the stronger signal from the loss side (Stokes) is counted as positive. The choice of laser energy (typically in the visible or near-infrared) does not affect the Raman shift, but if the laser energy is resonant with an electronic transition, the Raman intensity can be increased by many orders of magnitude. In a one-dimensional system such as carbon nanotubes where the density of states is strongly peaked, resonance Raman scattering dominates over non-resonant contributions. Hence, resonance Raman scattering from nanotubes gives information of the vibrational mode from the Raman shift, as well as of the optical transition energy since it is close to the energy of the laser.

This section is meant to give a brief background to resonant Raman scattering applied to carbon nanotubes and practical advice on how to do the measurements, while discussing some pitfalls to be aware of when interpreting data. While Raman scattering can be used for quantitative measurements, most standard measurements give relative and qualitative information that is best used for comparisons of similar samples in the same sample state (*e.g.*, in ropes, powders, solution, polymers, etc.)

The most prominent Raman active peaks in carbon nanotubes are the low frequency, radial breathing modes (RBM) and the higher frequency, D, G and G' modes (to be defined in Section 2 of this chapter). While D, G, and G' modes are also found in graphite, the RBM mode is a unique carbon nanotube mode. A study of the RBMs gives information regarding the distribution of nanotube diameters in a given sample. Due to the resonance behavior of the Raman intensity, several laser lines need to be used to determine the extent of the

diameter distribution. The relative strength and width of the D band mode also gives a qualitative measurement of how large a fraction of graphitic material and nanotubes with defects are present in the sample. Figure 4.1 shows Raman spectra from a high-pressure carbon monoxide (HiPCo) produced powder where the RBM, D, G and G' bands are shown.



**Figure 4.1.** Raman spectra of carbon nanotubes

## 4.1 Resonant Raman Scattering in Carbon Nanotubes

### Electronic structure

One of the more intriguing aspects of carbon nanotubes is they can be either metallic or semiconducting with variable and direct bandgap. Depending on the chirality ( $n,m$ ), the nanotubes are metallic when  $n-m = 3k$  ( $k$ =integer) and semiconducting otherwise. This essential feature of the electronic structure is readily obtained from considering the electronic structure of graphite and then applying chirality-dependent quantization of the allowed electron states in the confined directions. The one-dimensional electron bands lead to sharp peaks in the joint electronic density of states, the so-called van Hove singularities, which are labeled  $E_{ii}$  with  $i=1,2,3,\dots$  numbering the valence and conduction sub-bands (3-6). The singularities provide for strong resonant enhancement of the otherwise weak Raman signal. The  $E_{ii}$  is roughly proportional to  $1/\text{diameter}$  and are often plotted against the nanotube diameter, in what is called a Kataura plot.

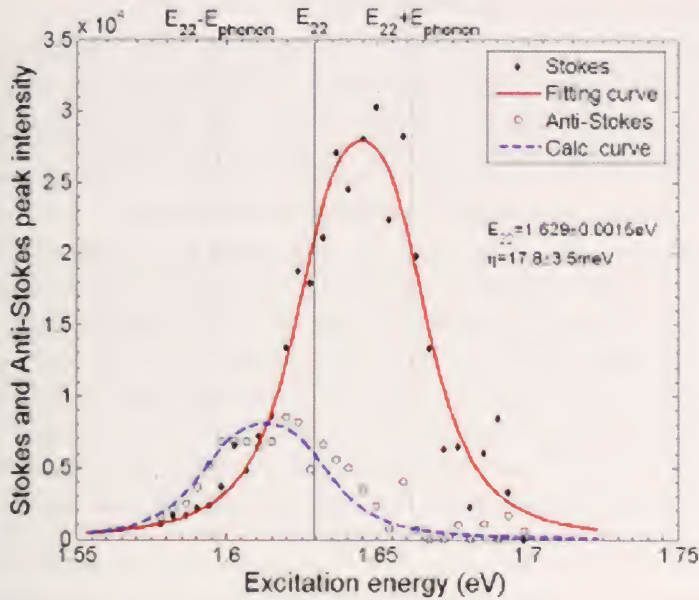
### Exciton versus band edge resonance

It has recently been demonstrated experimentally that optical transitions in nanotubes between the van Hove singularities are modified by electron-hole interaction with very large binding energies (7, 8). As is typical for a 1D system, the entire optical oscillator strength gets transferred from the band edge absorption  $E_{ii}$  to the exciton absorption energy,  $E_{ii} - E_{\text{binding}}$ . While this has far-reaching consequences for optically generated transport measurements, it does not significantly affect the analysis of resonant Raman scattering (9). The main difference is that the resonance occurs with the associated lowest bright exciton rather than the band edge energy  $E_{ii}$ . For simplicity, we will continue to refer to the optical transition energies as  $E_{ii}$  rather than excitons. However, it is important to keep in mind that the excitonic resonance energies are dependent on the tube's local environment. For example, screening effects change the energies for tubes in different environments, *e.g.*, dry powder versus individual tubes in solution or in air. Other environmental changes such as heating or cooling, strain, etc., also tend to shift the resonance energies. The implication is that a tube can move in and out of resonance by changing the environmental surroundings of the tube. For example, Raman signal from the (10,2) species is observed with a 785 nm laser line for a nanotube bundle, but the signal disappears when the tubes are dispersed in solution. Hence, the Raman signal will originate from a different subset of an ensemble when the environment changes sufficiently. Examples of how the resonance energy changes for individual tubes in solution and in bundles are shown in the appendix.

### Resonance Raman profile

Scanning the laser energy through an optical resonance gives the resonance excitation Raman profile for a given carbon nanotube phonon mode. Unlike photoluminescence excitation profiles where the center of the profile coincides with the optical transition  $E_{ii}$ , the Raman excitation profiles have two contributions; electronic resonance with the incoming laser light, ( $E_{\text{laser}} = E_{ii}$ ), and electronic resonance with the scattered light, which is shifted by a phonon-energy:  $E_{\text{scattered}} = E_{\text{laser}} \pm \hbar\Omega = E_{ii}$ . Hence, the center of the resonance profile is  $E_{ii} \pm \hbar\Omega/2$ .





**Figure 4.2.** Resonance excitation profile. The curves show the Stokes (red) and Anti-Stokes (blue) resonance excitation profiles for (9,4) individual nanotubes with RBM = 257  $\text{cm}^{-1}$  (15).

## 4.2 Raman-Active Modes in Carbon Nanotubes (RBM, D, G and G')

Carbon nanotubes have a rich Raman spectrum, but here we will only discuss the most well-known bands. For an extensive review of the Raman scattering from nanotubes, see (10). The parent material to carbon nanotubes is graphite, which has several phonon modes that are Raman active. The most prominent modes are the G-band (G-graphite), the D-band (D-disorder) and the G' band (second-order Raman scattering from D-band vibrations). In addition to the graphite modes, carbon nanotubes have a unique, prominent, phonon mode due to isotropic radial expansion of the tube, which is called the radial breathing mode (RBM). The RBM frequency is inversely proportional to the diameter of the tube, making it an important feature for determining the diameter distribution of a sample. Its absence in other graphitic forms makes it a useful diagnostic for confirming the presence of nanotubes in a sample. Below, each Raman-active mode will be discussed further.

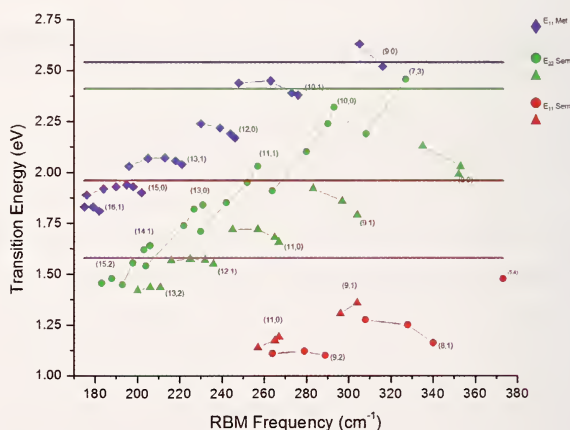
## 4.2.1 Radial Breathing Mode (RBM)

The RBM mode is the real signature of the presence of carbon nanotubes in a sample, since it is not present in graphite. The group theoretical notation is  $A_{1g}$  and it is often called the “breathing” mode. The RBM frequency ( $\omega$ ) is inversely proportional to the nanotube diameter with the relation

$$\omega(\text{cm}^{-1}) = A/\text{dia}(\text{nm}) + B(\text{cm}^{-1})$$

where the constants A and B have been determined experimentally with  $A = 223 \text{ cm}^{-1}/\text{nm}$ ,  $B = 10 \text{ cm}^{-1}$ . Several groups have found slightly different best fits of A and B, but for tube diameters between (0.8 to 1.3) nm, they give nearly identical frequency-diameter results. Most experimental systems that use a single grating spectrometer with a holographic notch filter for laser line rejection are limited to Raman frequencies larger than (100 to 120)  $\text{cm}^{-1}$ , which restricts the range of diameters that can be measured to smaller than  $\approx (2 \text{ to } 2.5) \text{ nm}$ . The use of multi-grating systems can lower the possible observed frequencies, thereby permitting larger tubes to be studied.

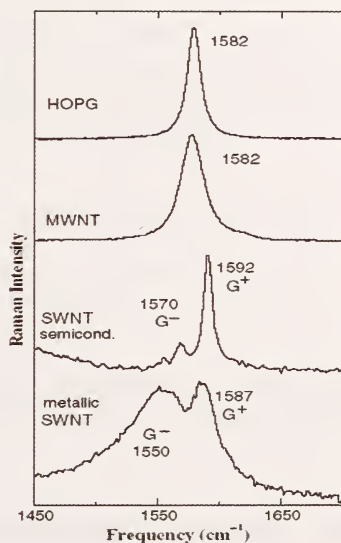
Several groups have mapped the transition energy versus radial breathing mode frequency (Energy vs.  $1/\text{diameter}$ ) to form the Raman equivalent of the Kataura plot (Energy vs. diameter) (11-14). Knowledge of the diameter and resonance energy  $E_{ii}$  makes it possible to separate the RBM signatures of metallic tubes from semiconducting tubes using the Kataura plot ( $E_{ii}$  vs diameter), and for



small diameter tubes where there are fewer chiralities / diameter, it may be possible to assign the chirality from resonant Raman spectra. Figure 4.2 shows an experimentally determined plot for individual nanotubes in solution for  $E_{11}$  and  $E_{22}$  semiconducting and  $E_{11}$  metallic transitions (15). While it is possible to pair RBM frequencies with  $E_{ii}$  obtained from full Raman excitation profiles to arrive at a nearly unambiguous chirality assignment for a specific RBM, the Kataura plot may be used to help in assigning RBM features obtained in single excitation line spectra. The horizontal lines in Figure 4.3 show commonly used laser line energies: Ar-ion 488 nm (blue), 514.5 nm (green); HeNe 632.8 nm (red); and Ti-Sapphire 785 nm (magenta). The resonance window, which determines which specific chiralities will appear in a RBM spectrum excited at a given excitation wavelength, will depend strongly on the environment and varies from tens of meV for a single nanotube to  $>140$  meV for nanotubes in bundles. RBMs from nanotubes outside the resonance window of a selected excitation wavelength will not be observed. Furthermore, the resonance energies have been observed to shift depending on environment due to screening, with the highest resonance energies found for individual nanotubes in air, (10 to 30) meV lower for individual nanotubes in solution and  $\approx 100$  meV lower for nanotubes in bundles.

#### 4.2.2 The G Band

The G mode is a tangential shear mode of the carbon atoms. In graphite, there is one single G mode at  $\approx 1580$   $\text{cm}^{-1}$ . In carbon nanotubes, the single G band transforms into several modes due to the confinement of wave-vectors along the circumference. For chiral tubes, the G-band is composed of six modes with symmetries  $A_{1g}$ ,  $E_{1g}$  and  $E_{2g}$  (two of each). The frequency of the higher energy branch,  $G^+$  does not vary with diameter, while the low energy branch,  $G^-$  gets softer for smaller diameter nanotubes. Examples of G-band structure from different carbon-based materials are shown in Figure 4.4, from (16).

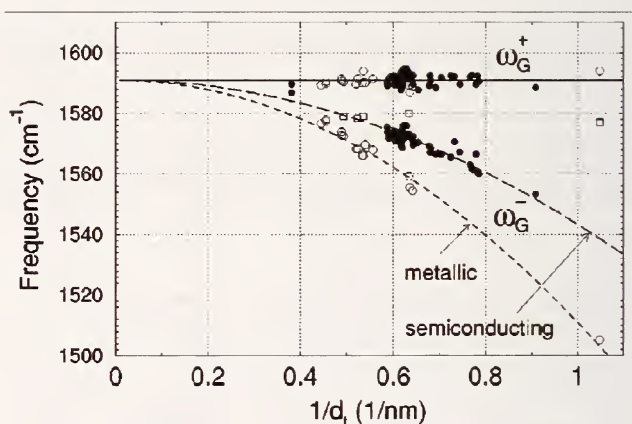


**Figure 4.4.** From (16). G bands for graphite (HOPG), multiwall CNTs (MWNT), semiconducting and metallic SWNTs.

**Semiconducting nanotubes:** The highest mode,  $G^{+}= (1590 \text{ to } 1595) \text{ cm}^{-1}$  is a longitudinal optical (LO) shear mode parallel to the axis of the nanotube. Transverse optical (TO) shear modes perpendicular to the tube axis,  $G^-$  modes, are softened due to the curvature or smaller diameters, and the frequency depends on the

tube diameter. The G band line shapes are Lorentzian and relatively narrow even in a bundle for defect-free nanotubes ( $\text{FWHM} \approx 11 \text{ cm}^{-1}$ ).

**Metallic nanotubes:** The metallic tubes are easily recognized from the broad and asymmetric Breit-Wigner-Fano line-shape of the G<sup>-</sup> band. The frequency down shift of the G<sup>-</sup> is particularly strong for metallic nanotubes, with down shifts of the G<sup>-</sup> mode of  $\approx 100 \text{ cm}^{-1}$  for small diameter tubes. The G<sup>-</sup> energy decreases with decreasing diameter faster than for semiconducting nanotubes while the G<sup>+</sup> remains essentially constant in frequency; see Figure 4.5 (17). The line-shape was initially attributed to coupling between the G<sup>-</sup> phonons with low-lying optical plasmon corresponding to the tangential motion of the electrons on the nanotube surface. Recent work instead suggests that the coupling is due to a resonance between phonons and electron-hole pairs and that the assignment of the axial and circumferential assignments are reversed for metallic tubes, *i.e.*, that the lower energy G<sup>-</sup> is a LO (axial) phonon mode (18).



**Figure 4.5.** From (17) Measurements showing the diameter dependence of the G- band for metallic and semiconducting nanotubes

## 4.2.3 Second Order Raman scattering, the D and G' Modes (Zone Boundary Phonons)

The D and G' modes originate from longitudinal optical (LO) phonons from the vicinity of the K-point in the (graphene) Brillouin zone. The Raman D and G' are second order processes that involve e-phonon scattering from  $\mathbf{k} + \mathbf{q}$  via the zone boundary LO phonon, and scatters back to the  $\mathbf{k}$  state either elastically via a defect (D band) or inelastically via a second LO phonon, and emits a photon by recombining with a hole at a  $\mathbf{k}$  state.



**The D band:** The D- band is called a defect mode because a defect is needed to elastically scatter in order for the process to conserve momentum. The second order scattering described above can either be due to phonon-defect or defect-phonon scattering which yields two Raman peaks of slightly different energies. The quality of a sample is often evaluated by comparing the D to G band intensity, or the D to G' intensity. For high-quality samples, without defects and amorphous carbon, the D/G ratio is often below a couple of percent. Examples of such low D/G ratios can be found in CVD-grown nanotubes (19) and in high-quality laser oven-grown nanotubes (20).

Since different nanotubes have different resonance energies, the D band frequency is not fixed for different laser energies. Table 4.1 gives approximate values for four different laser lines. The D band is present in all carbon allotropes, including amorphous  $sp^2$  and  $sp^3$  carbon. The D band signal can originate from nanotubes with defects and/or from non-SWNT carbon. One way to identify the different contributions is by the line-shape of the D-band, where a broad peak ( $\approx 100 \text{ cm}^{-1}$ ) is indicative of amorphous carbon. The d-band width for nanotube ensembles are  $\approx (10 \text{ to } 20) \text{ cm}^{-1}$ .

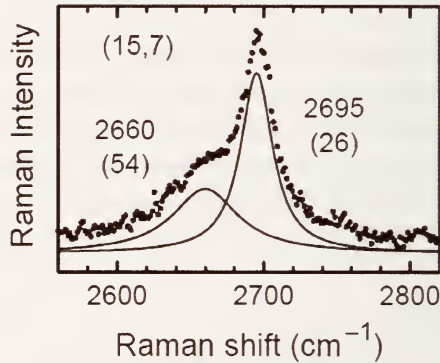
Figure 4.10 (Section 6 of this Chapter) in the Appendix shows the D and G band in double wall carbon nanotube powder before and after optical heating. The heating has removed much of the defect-rich carbon nanotubes and amorphous carbon as is evidenced from reduction of the D band intensity.

Laser line (nm/eV)	785 / 1.58	633 / 1.96	514 / 2.41	488 / 2.54
D-band ( $\text{cm}^{-1}$ )	$\approx 1290$	$\approx 1330$	$\approx 1345$	$\approx 1360$

**Table 4.1.** Approximate values for D band Raman shift with different laser excitation energies.



**The G' Band:** The G' band at frequencies (2500 to 2900)  $\text{cm}^{-1}$  is the second order process from two zone boundary LO phonons with wave vectors  $q$  and  $-q$ , thus automatically preserving the momentum conservation constraint. Therefore, the G' band is an intrinsic property of the nanotube and graphite, and present even in defect-free nanotubes where the D band is completely absent. The frequency of the G' band is close to twice the D-band frequency. The dispersion of the G' band is  $\omega_{G'} \sim 2420 \text{ cm}^{-1} + 105 \text{ cm}^{-1}/E_{\text{laser}} (\text{eV})$ .



**Figure 4.6.** a) 2 G' peaks from a (15,7) nanotube where the incident EL = 2.41 eV and the scattered EL - EG = 2.08 eV light. The resonant energies are  $E_{33} = 2.19 \text{ eV}$  and  $E_{44} = 2.51 \text{ eV}$ . From (21).

**Incoming and Outgoing (Scattered) Resonances:** The energy of a G' band is substantial, ( $\approx 0.33 \text{ eV}$ ). In ensemble measurements, nanotubes can be resonant either with the incoming laser energy, or with the (lower) scattered energy, and both scattering events will contribute to the signal. Incoming and outgoing scattering resonances will result in G' bands at different energies due to the energy dispersion of the G' band. Sometimes, the incoming and scattered light matches a nanotube electronic structure so well that the incoming and scattered light can both be resonant with two different  $E_{ii}$ 's from one particular nanotube. In this case, two G' peaks at different energies are observed from the same nanotube, due to the energy dispersion of the phonon modes near the zone boundary as is illustrated in Figure 4.6 (21).

### 4.3 Width of the Resonance

It is of interest to know the width of the resonance to determine how far away from a resonance it is possible to get a Raman RBM signal. The incoming resonance is peaked around  $E_{ii}$ , and the outgoing resonance is a phonon energy higher (Stokes) or lower (anti-Stokes). The width of the resonance window is approximately the sum of the RBM energy + the resonance broadening  $\gamma$ .

#### *Ensemble measurements (11-14)*

- *Solution:* The broadening  $\gamma$  has been measured to be  $\gamma \approx 60$  meV for nanotubes dispersed in sodium dodecyl sulfate solution.
- *Bundles:* For nanotubes in thick bundles the broadening is  $\gamma \approx 120$  meV.

#### *Individual measurements (15)*

- For (nearly) individual nanotube measurements suspended in air or on substrates, the width  $\gamma$  varies from  $\gamma = (10 \text{ to } 40)$  meV.

### 4.4 Strength of the Raman Signal; Electron–Phonon Coupling

Apart from the electronic resonance condition that controls the strength of the Raman signal, the peak intensity also depends on the electron-phonon (e-ph) coupling. This is an active area of research with constant updates in the literature. Both measurements and calculations agree that there is a strong chirality and diameter dependence of the e-ph coupling for the radial breathing modes as well as a dependence on which  $E_{ii}$  is active. For semiconducting nanotubes, the Raman scattering cross-section is proportional to

$$|M_{e-ph}|^2 = \left| \frac{a(E_{ii})}{d_t^2} + n \frac{b(E_{ii})}{d_t} \cos 3q \right|^2$$

where the constants  $a$  and  $b$  depend on which electronic energy level  $E_{ii}$  is excited,  $v$  is the chiral index  $-1$  or  $1$  (22). Hence, when determining chirality distributions from Raman RBM intensities one has to take into account the chirality dependent e-ph coupling strength (13, 15, 23, 24).

## 4.5 Depolarization and Selection Rules

The largest Raman intensity will be generally observed for light polarized along the tube axes, and almost no signal will be observed for cross-polarized light. The intensity varies as  $\cos^4\theta$ , where  $\theta$  is the relative angle between the electric field,  $E$ , and the nanotube axis. The angular dependence can be used to measure the degree of alignment, *e.g.*, carbon nanotubes dispersed in a polymer matrix.

The decrease in signal for polarization perpendicular to the nanotube axis is due to depolarization or the antenna effect. Light with an external electric field vector parallel to the nanotube axis,  $E_{\parallel}$ , does not induce a polarization, and the total field is equal to the external field. On the other hand, an electric field perpendicular to the nanotube axis,  $E_{\perp}$ , induces charges on the two opposing sides of the wall. The effect is a large opposing depolarization field that reduces the external field  $E_{\perp}$ . The antenna effect is a strong effect for narrow nanotubes  $<2$  nm.

The resonance with the  $E_{ii}$  transition for light polarized parallel to the nanotube axis is due to angular momentum conservation which requires  $\Delta m=0$  for  $E_{\parallel}$  where  $m$  is the angular momentum quantum number. For a perpendicular field  $E_{\perp}$  the angular momentum conservation requires  $\Delta m=\pm 1$ , *i.e.*,  $E_{ij}$  with  $j=\pm 1$ . Due to the depolarization effect,  $E_{ii}$  transitions are favored over  $E_{ij}$  transitions.

## 4.5 Practical Considerations

### 4.5.1 Measurement Setup

A variety of commercial Raman instrumentation is available for characterization of nanotube samples. Instrumentation ranges from relatively inexpensive ( $\approx \$10,000$ ) fixed wavelength benchtop systems with common excitation wavelengths of 532 nm, 633 nm, or 785 nm. Higher sensitivity single wavelength systems based on high-throughput spectrographs incorporating holographic diffraction gratings and notch filters are also available at higher cost. For studies of single nanotubes in very disperse samples, micro-Raman instrumentation is used which consists of a microscope coupled to a spectrometer with a CCD camera and one or more laser excitation sources.

More versatile scanning Raman systems may be assembled from commercially available triple spectrographs coupled to tunable excitation sources such as Ti:Sapphire and dye lasers. Similar excitation tunability may be coupled to micro-Raman systems.

In all systems, the spectrometer grating should be chosen to have a large throughput for the laser line(s) used, and to give the desired spectral resolution, preferably  $3\text{ cm}^{-1}$  or better.

## Calibration and Alignment

If several laser lines are used it is necessary to re-align optical paths and calibrate the frequencies after each line switch, and the practitioner should follow standard alignment procedures.

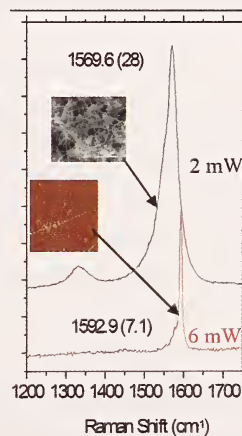
Before each set of measurements a quick check of alignment and calibration should be done:

Calibration of grating reading:

- Check that the Stokes and anti-Stokes peak frequencies are symmetric around the laser line for the test sample.
- A general calibration is needed with well-known lamp lines, such as those from helium, neon or krypton for absolute frequency measurements and to assign the spectral resolution. These can be compared with known values found at [http://physics.nist.gov/PhysRefData/ASD/lines\\_form.html](http://physics.nist.gov/PhysRefData/ASD/lines_form.html). Other Raman shift standards such as acetamidophenol (Tylenol) or cyclohexane may also be effectively used for spectral calibration. See the McCreery group website: <http://www.chemistry.ohio-state.edu/~rmccreer/freqcorr/shift.html>
- For tunable laser sources, an optical wavemeter can be used to calibrate the laser energy.

Optical path alignment for micro-Raman instruments:

- Adjust the excitation path so that the laser light goes straight through the objective: when adjusting the z-position in and out of focus, the laser spot should expand symmetrically. If not, the spectral calibration will be off and collection efficiency lowered.
- Use a calibration sample with a strong and well-known Raman line, *e.g.*, the  $\approx 521\text{ cm}^{-1}$  Raman line from polished silicon (100). Align the Si (110) direction with the laser polarization. Check that the Si Raman signal is maximized for a given wavelength, laser power and slit width. Record the signal per second for a specific power for comparison.



**Figure 4.7.** G band from powder and from individual nanotube on substrate. Heating effects are clearly seen for the powder where the G band is down shifted  $23\text{ cm}^{-1}$  while the single tube is unaffected at 3 times the power.



### 4.5.2 Laser Power Heating Effects

It is relatively easy to unintentionally heat the sample by optical heating, especially when using a Raman microscope, in which the laser light is focused to a small focal volume with a resulting high power density. Optical heating of the sample could possibly damage the sample by burning, and also change the resonance energies which decrease with temperature. Therefore, sufficient sample heating will result in resonance with a different subset of the sample, and yield different spectra at different temperatures. It is only when a (nearly) single nanotube is studied that one can determine the actual effect of heating on the Raman spectra. For bulk measurements, any change is convoluted by resonances with a different subset of nanotubes in the sample. The laser powers that can be safely used without significant heating depend both on laser energy and on sample preparation as discussed below. More details are given on this topic in the Appendix (section 6 of this chapter).

#### Diagnostics

The  $G^+$  mode frequency can be used as a thermometer. In the literature, frequency shifts of the  $G^+$  mode with temperature from  $(-0.022 \text{ to } -0.048) \text{ cm}^{-1}/\text{K}$  have been reported. To avoid excessive heating, the power should be lowered until the  $G^+$  stays constant in energy.

The Stokes/anti-Stokes intensity ratio for the radial breathing modes is also an indicator of the temperature, and a change in this ratio with laser power is also an indication of excess laser heating. However, this ratio is more complex to interpret since the ratio depends both on temperature and the resonance energy. For example, if  $E_{\text{laser}} \pm E_{\text{ii}}$  at  $T_1$  and the temperature increased to  $T_2$ , the change in resonance condition will tend to decrease the IAS/IS ratio while the Boltzmann factor favors an increase in the  $I_{\text{AS}}/I_{\text{S}}$  ratio with increasing temperature.

#### Sample Type

The physical state of the sample (and the degree of impurities) plays a large role in choosing a suitable laser power. Samples with a higher degree of graphitic impurities heat more easily, presumably since the effective thermal conductivity of the graphitic impurities are not as high as for nanotubes, see Figure 4.7.

Individual nanotubes dispersed in solution with a surfactant will heat significantly less than a dry powder/ bundles in air, and individual nanotubes on a substrate are also efficient in dissipating heat. The heating of nanotubes in a polymer matrix will depend on the degree of dispersion of the nanotubes and heat conductivity and heat capacity of the polymer.

We recommend using  $< 3 \times 10^5 \text{ W/cm}^2$  for samples in solution and for individual nanotubes on a substrate, and  $< 10^4 \text{ W/cm}^2$  for powders and dispersions in polymers and to check whether a decrease in power will further shift the  $G^+$  band frequency.

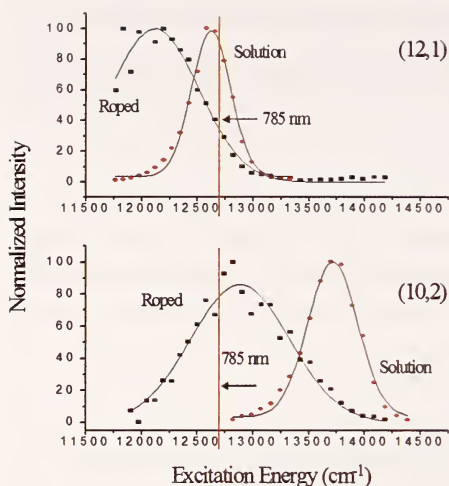
### 4.5.3 Material Inhomogeneity

Carbon nanotube powder varies in composition on a micrometer scale. Therefore it is recommended that several spectra are collected from different sample positions to get a statistically meaningful measurement. A second approach is to collect signal from a larger area.

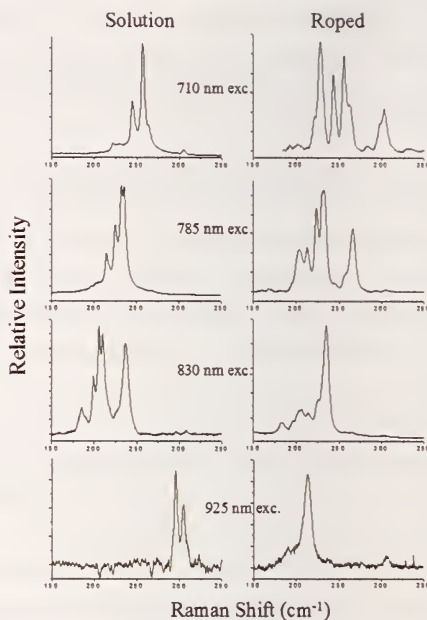
### Sample Preparation

Since environment and the degree of nanotube aggregation will influence excitation window, excitation energy and degree of heating, it is necessary to prepare samples that will be compared in the same way. Whether raw, dry material, or formed into a pellet, or dissolved into solution, or dispersed on filter paper, or isolated, each sample preparation brings its own unique features to the Raman spectra and therefore should be considered during analysis.

**Solution preparation:** Typical preparation of solution samples of nanotubes begins with high shear mixing of the nanotubes in a 1 % aqueous solution of surfactant. The suspension is then ultrasonicated at high power with tip or cuphorn sonicators (typically for 10 min). Samples are then ultracentrifuged. Four hour centrifuge times work well, with acceleration force chosen depending on nanotube production method. For HiPco nanotubes, an acceleration force of 110,000 g works well, while lower forces (60,000 to 70,000) g work better for samples with small diameter distributions (such as those produced in the cobalt-molybdenum catalyst (CoMoCAT) based process. Centrifuged samples will show separation between pelleted aggregates (found at the bottom of the centrifuge tube) and individualized nanotubes, which are decanted off. Common surfactants are sodium dodecyl sulfate (SDS), sodium dodecylbenzene sulfate (SDBS), sodium cholate, and even direct suspension into single or double stranded DNA. SDBS is known to give the most blue-shifted excitation spectra of any of the listed surfactants. For large-diameter nanotubes, such as those produced in laser-oven methods, sodium cholate or polymeric surfactants (such as Triton-X 100 or Pluronic) may be most suitable for sample suspension. Solution spectra are readily obtained from samples contained in nuclear magnetic resonance or melting point capillary tubes.



**Figure 4.8.** Comparison of Raman excitation profiles of SDS solubilized and bundled nanotubes for the (12,1) and (10,2) chiralities. The vertical line represents the 785 nm excitation line position.



**Figure 4.9.** Comparison of RBM spectra for SDS solubilized and bundled nanotubes at four specific excitation wavelengths.

## 4.6 Appendix

### 4.6.1 Illustration of Aggregation Effects

As noted above, sample state and environment will have a significant effect on features observed in SWNT Raman spectra, particularly in the RBM region. These effects are primarily due to shifting and broadening of the electronic transitions. These effects are most pronounced in comparing solution to aggregated samples. Figure 4.8 illustrates the significant red-shifting and broadening of excitation profiles for the (12,1) and (10,2) chiralities that occur upon nanotube bundling. As seen in Figure 4.9, such changes in excitation spectra can lead to very different features appearing in RBM spectra at a given excitation wavelength.

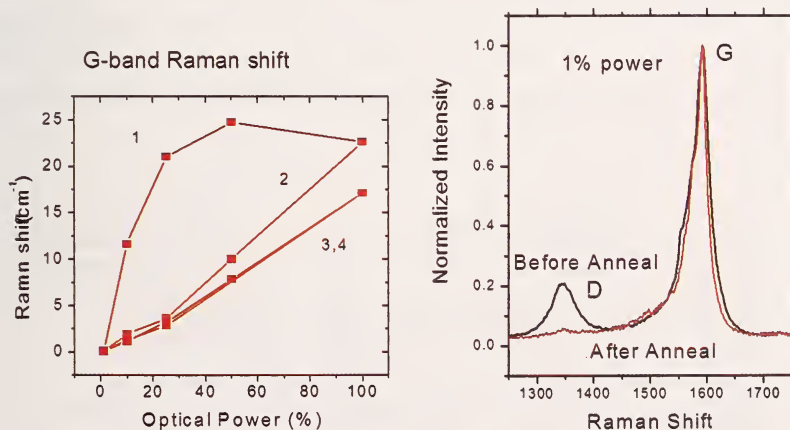
Such effects underscore the importance of understanding the effects of electronic perturbation on observed RBMs. This is particularly relevant to the use of Raman for characterization of separation processes. Care must be taken to ensure that observed changes in relative RBM intensities are not incorrectly attributed to changes in relative populations of their corresponding chiralities, when the cause may instead be a shift in electronic transition energies that

brings a different set of chiralities into resonance with a specific excitation wavelength.

As illustrated in Figs. 4.8 and 4.9, the use of 785 nm excitation can be a practical means for probing the extent of nanotube aggregation. Bundling of nanotubes results in increased enhancement of the (10,2) RBM at  $265\text{ cm}^{-1}$ , relative to nearby RBMs (including the (12,1) mode at  $236\text{ cm}^{-1}$ ), producing the so-called roping peak. Note that, while the (10,2) RBM at  $265\text{ cm}^{-1}$  is strongly observed only in the bundled sample with 785 nm excitation, the (12,1) RBM at  $236\text{ cm}^{-1}$  appears strongly enhanced in both sample types. This behavior results from the different resonant excitation conditions experienced by the two chiralities. As seen in Figure 4.8, 785 nm excitation is near the peak of the excitation profile for the individualized (12,1) nanotubes, but is well away from the resonance window for the (10,2) in solution. Thus, the (12,1) RBM is observed but not the (10,2). Bundling-induced red-shifting places the 785 nm excitation near the peak of the (10,2) transition, while significant intensity in the tail of the (12,1) profile still remains. Therefore, for bundled samples, both the (12,1) and (10,2) chiralities will be observed.

#### 4.6.2 Illustration of Heating Effects

Figure 4.10 shows the effects of optically heating a sample of double wall carbon nanotube powder. As the optical power is increased, the G band is



**Fig 4.10.** Effect of optical heating of a powder sample. G band Raman shift indicative of optical heating of DWNT powder using 514 nm laser. 100 % power = 8 mW with NA=0.8 objective. A) Down-shift in the G+ mode as a function of optical power. The numbers indicate the time sequence of the measurements B) Raman spectra at low power (no heating) before and after thermal cycling shows the reduction of the D band intensity and line-width after heating.

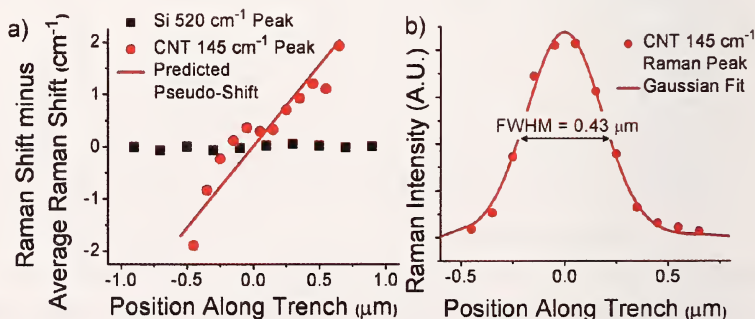


dramatically shifted down in frequency due to heating. Here 100 % power corresponds to 8 mW optical power at 514 nm with a  $NA=0.8$  objective ( $\approx 10^6$  W/cm<sup>2</sup>). The maximum shift of the G band corresponds to a sample temperature increase of  $\approx 480$  °C using the most conservative estimate of 0.048 cm<sup>-1</sup>/K. Subsequent cycles of increasing and decreasing the optical powers show a less marked heating than the first increase, Fig 4.10 A. This behavior can be correlated to the removal of carbon impurities and nanotubes with defects shown in Fig. 4.10 B), which shows the reduction in the D-band intensity after the local optical heating.

The D-band disappears as the temperature is increased, and during subsequent power cycling the temperature increases less. These results illustrate that a sample with large D-band tends to heat more readily than a more ideal nanotube sample, and that heating can remove the defects, either by annealing defects or the physical “burn off” of the defective material.

## 4.6.3 Measurements from One Individual Nanotube - “Nano-Slit Effect”

In confocal microscopy, a pinhole is used in the image plane of the microscope system to limit the area and the depth from which the signal is collected from the sample. Confocal techniques are used for mapping an image at different depths (confocal sectioning), *e.g.*, mapping nanotube composite depth profiles, although the penetration depth will limit the depth information that is possible to extract. When confocal microscopy is used from a sparse sample, the nano-scaled object will act as a “nano-slit”, and a slight displacement of the nano-particle from the optical axis will lead to false shifts in the measured Raman frequency.



**Figure 4.11.** A) from (15) False Raman shift as a function of horizontal displacement of a single nanotube (in red). B) Measurement of the optical beam profile at the focal plane using a nanotube.

Knowing the resolution of the spectrometer, detector pixel size, and the overall magnification from object plane to detector, this “pseudo-shift” is easily calculated for a given distance in the spectral direction of the emitter from the optical axis.

The “nano-slit” effect is illustrated in Fig 4.11 A) by measuring the shift RBM frequency as a function of position stepping across the nanotube oriented parallel to the groove direction of the spectrometer grating. For comparison, the silicon  $521\text{ cm}^{-1}$  Raman peak from the substrate is also shown. The silicon signal originates from all points illuminated by the beam spot and is unaffected by translation and consequently does not shift with sample position.

The “nanoslit” configuration also provides an elegant method for directly measuring the profile of the beam intensity in the object plane. An example is shown in Fig. 4.11 B).

## Acknowledgements

We would like to thank Angela Hight-Walker of NIST, Gaithersburg, Apparao Rao of Clemson University and Victor Hadjiev of University of Houston for critical reading of the manuscript. Special thanks to Sivaram Arepalli at NASA-Johnson Space Center and Steve Freiman of NIST for coordinating the effort, and for their continuous support and advice.

## Literature Cited

1. Ferraro J. 2002. Introductory Raman Spectroscopy Academic Press
2. Smith E, Dent G. 2005. Modern Raman Spectroscopy Wiley
3. Dresselhaus MS, Dresselhaus G, Jorio A. 2004. *Annual Review of Materials Research* 34:247-78
4. Kataura H, Kumazawa Y, Maniwa Y, Umezu I, Suzuki S et al. 1999. *Synthetic Metals* 103:2555-8
5. Reich S, Thomsen C, Maultzsch J. 2004. Carbon Nanotubes: Basic Concepts and Physical Properties Wiley
6. Saito R, Dresselhaus G, Dresselhaus MS. 1998. Physical Properties of Carbon Nanotubes Imperial College Press
7. Maultzsch J, Pomraenke R, Reich S, Chang E, Prezzi D et al. 2005. *Physical Review B* 72:
8. Wang F, Dukovic G, Brus LE, Heinz TF. 2005. *Science* 308:838-41
9. Vamivakas AN, Walsh A, Yin Y, Unlu MS, Goldberg BB, Swan AK. 2006. *Physical Review B* 74:
10. Dresselhaus MS, Dresselhaus G, Saito R, Jorio A. 2005. *Physics Reports-Review Section of Physics Letters* 409:47-99

11. Doorn SK, Heller DA, Barone PW, Usrey ML, Strano MS. 2004. *Applied Physics A-Materials Science & Processing* 78:1147-55
12. Fantini C, Jorio A, Souza M, Strano MS, Dresselhaus MS, Pimenta MA. 2004. *Physical Review Letters* 93:
13. Maultzsch J, Telg H, Reich S, Thomsen C. 2005. *Physical Review B* 72:
14. Telg H, Maultzsch J, Reich S, Thomsen C. 2006. *Physical Review B* 74:
15. Yin Y, Walsh AG, Vamivakas AN, Cronin SB, Stolyarov AM et al. 2006. *Ieee Journal of Selected Topics in Quantum Electronics* 12:1083-90
16. Jorio A, Pimenta MA, Souza AG, Saito R, Dresselhaus G, Dresselhaus MS. 2003. *New Journal of Physics* 5:
17. Jorio A, Souza AG, Dresselhaus G, Dresselhaus MS, Swan AK et al. 2002. *Physical Review B* 65:
18. Lazzeri M, Piscanec S, Mauri F, Ferrari AC, Robertson J. 2006. *Physical Review B* 73:
19. Doorn SK, Zheng LX, O'Connell MJ, Zhu YT, Huang SM, Liu J. 2005. *Journal of Physical Chemistry B* 109:3751-8
20. Dillon AC, Parilla PA, Alleman JL, Gennett T, Jones KM, Heben MJ. 2005. *Chemical Physics Letters* 401:522-8
21. Souza AG, Jorio A, Swan AK, Unlu MS, Goldberg BB et al. 2002. *Physical Review B* 65:
22. Goupalov SV, Satishkumar BC, Doorn SK. 2006. *Physical Review B* 73:
23. Jorio A, Santos AP, Ribeiro HB, Fantini C, Souza M et al. 2005. *Physical Review B* 72:
24. Luo ZT, Papadimitrakopoulos F, Doorn SK. 2006. *Applied Physics Letters* 88:

## 5 Optical, Electron and Probe Microscopy

**Cheol Park and Peter Lillehei, NASA Langley Research Center, Science and Technology Corporation Hampton, VA, and National Institute of Aerospace, VA**

### 5.1 General Description

The development of tools to assess the dispersion of nanotubes in polymer matrices is based on the premise that one cannot improve what cannot be measured. An accurate assessment of the dispersion is the most critical factor in correlating the behavior of the final nanotube polymer composites to the nanostructure. This guide outlines the tools and the procedures used to assess the dispersion of nanotubes in a polymer matrix to allow for improvement and tailor-ability of the multifunctional properties of the composites.

### 5.2 Introduction

The biggest challenge in translating the multifunctional properties of nanotubes into improved composite structure performance is the difficulty in achieving an effective dispersion of the nanotubes in a polymer matrix (1-7). A new set of characterization techniques is required to assess nanotube dispersion in polymer matrices. The work presented herein lays a foundation for the systematic characterization of carbon nanotube composites via optical, electron, and probe microscopy.

Spectroscopic tools such as UV-VIS, IR, and Raman aid characterization by providing information on tube structure, functionalization, charge transfer between the polymer and the nanotubes, and even alignment of the nanotubes within the matrix (8-10). However, these techniques are optically based and, thus, sample an ensemble of nanotubes because the minimum spot size is on the order of a few microns even in state-of-the-art instruments. While this information is useful and necessary to help understand the electrical, mechanical, and thermal data collected on the composites, additional information on how the nanotubes are actually being distributed within the polymer matrices is necessary to better understand the nanocomposite morphologies. This has led to the effort to develop these visual techniques to complement the optical spectroscopic techniques already commonly used to characterize nanotubes and nanocomposites.

The procedures used to assess dispersion of nanotubes in polymer matrices are outlined in Fig. 5.1. The sample is first examined by optical microscopy to determine if any large-scale agglomerations are present. Figure 5.2 shows typical examples of optical micrographs of undesirable dispersion with SWNT aggre-



gates and desirable uniform dispersion. If the sample passes optical microscopy standards, it is characterized as being optically dispersed (Figure 5.2b). It is then sufficient to state that the sample does not have any visual aggregation on the scale of approximately 1  $\mu\text{m}$  or larger. To assess the aggregation, bundling, alignment, and local concentration gradients on a scale below 1  $\mu\text{m}$  requires electron and probe microscopy techniques. These techniques include scanning electron microscopy (SEM), transmission electron microscopy (TEM), and scanning probe microscopy (SPM). Defining the quality of the dispersion on a scale below 1  $\mu\text{m}$  is subjective. To suggest that a sample with 500 nm bundles is well dispersed would be misleading; therefore this guide outlines a procedure for the accurate assessment of bundle size, presence of agglomerations, and local concentration gradients on the scale below 1  $\mu\text{m}$ .

The following sections describe the procedures and data that can be gleaned from the analytical techniques used, with a discussion pertaining to the limits of data interpretation. This will serve as a foundation for a robust and quantifiable nanotube composite characterization and will establish the limits for each analytical method.

### **5.3 Experimental Description**

#### **5.3.1 Instrumentation**

##### **Optical Microscopy**

The optical microscope typically employs the use of light in the visible spectrum to generate a micrograph. Illumination of the samples above or below the sample determines the imaging mode, either reflection or transmission respectively. Ultraviolet illumination, polarizers, bright field/dark field imaging and optical filters enable enhanced imaging techniques.

##### **Scanning Electron Microscopy**

A scanning electron microscope employs the use of high-energy electrons, rather than photons, to image a surface. The sample must have a moderate electrical conductivity and be stable in a high vacuum environment. Some new environmental scanning electron microscopes can handle low vacuum and high efficiency in-lens detectors can handle low conductivity samples, but for the most part conductivity and high vacuum stability is a requirement. The primary electron beam is scanned over the surface generating secondary electrons (SE), backscattered electrons (BSE), and Auger electrons, in addition to x-rays. The Auger electrons and x-rays can be collected to give spectroscopic or chemi-

cal identification. The SE are collected to generate the topographical images. BSE are used generate maps based on atomic number. As the primary beam is scanned its position is mapped with respect to the number of SE, BSE, Auger electrons and x-rays recorded at their respective detectors.

### Transmission Electron Microscopy

Transmission electron microscopes use a much more intense electron beam when compared to the beam used in SEM. These can be in the range of (200 to 300) keV for most commercial instruments. The collection of the SE, BSE, Auger electrons and x-rays can be achieved just as in SEM, but in addition the electron beam that passes entirely through the sample can be collected generating a transmission electron image. These electrons can be filtered based on how much energy was lost to the sample allowing for an additional spectroscopic technique. The scanning and transmission electron microscope's use of an electron beam to image a sample is a much higher resolution technique, when compared to optical microscopy, due to the much smaller characteristic wavelength of the electrons compared to the wavelength of visible photons. TEM, being the highest resolution technique, is typically capable of imaging samples up to atomic resolution.

### Scanning Probe Microscopy

Scanning probe microscopes are a family of microscopes that have the following modes of operation: scanning tunneling microscopy (STM), atomic force microscopy (AFM), magnetic force microscopy (MFM), electric force microscopy (EFM), tunneling AFM (TUNA), current sensing AFM (CSAFM), magnetic resonance force microscopy (MRFM), electron spin resonance STM (ESR-STM), near field scanning optical microscopy (NSOM), and others. In all cases a small probe is scanned in close proximity to or in contact with a sample. Depending on the technique different aspects of the sample can be interrogated. STM uses an atomically sharp Pt or W probe in close proximity to a conductive sample under bias to record the tunneling current between the sample and the probe. AFM, MFM, EFM, TUNA and CSAFM use a MEMS based probe positioned in the near field to record the topography, magnetic field, electric field and tunneling current and current flow respectively. Spectroscopic data can be recorded in the advanced techniques such as MRFM and ESR-STM. NSOM also uses a MEMS based probe but can collect optical and spectroscopic data simultaneously.

### 5.3.2 Contrast generation

To assess the dispersion of nanotubes within a polymer matrix requires a method of generating contrast between the SWNT and the various polymer matrices. Regardless of the techniques used at least one single attribute of the nanotubes that differs from the host polymer is exploited in a manner to generate contrast between the nanotubes and the matrix. Whether it is optical transparency, electrical conductivity, or some other physical property of the nanotubes that differ from the polymer, contrast is generated between the polymer and the tubes by mapping the variations in the composite based on these properties.

Optical microscopy techniques are particularly valuable for assessing poor dispersion rapidly. Contrast is generated between the nanotubes and the polymer due to vastly different optical properties of the nanotubes and the host polymer. In either transmission or reflection the dispersion of the nanotubes on a large scale greater than  $1\text{ }\mu\text{m}$  is easily assessed. Dispersion of the SWNT into aggregates or bundles smaller than the diffraction limit in the visible light range generally requires the use of electron and probe microscopy.

Contrast in SEM is due to the vastly different levels of conductivity of the SWNT and the polymer matrix. The composite builds up a charge from the primary electron beam and a stable electric field is generated on the surface of the sample. If the nanotubes are part of an electrical percolation network, they will dissipate the charge and lower the field to a less negative potential. If the electric field is stable, the percolation network can be imaged. Nanotubes disrupt the field in the surrounding polymer and appear as dark regions against the bright polymer matrix. Nanotubes at or near the surface, or penetrating into a cross-section, generate their own secondary electrons and appear as bright filaments in the image. This is shown in Figure 5.3 where SWNTs penetrate into a film and reverse contrast from bright to dark as they enter the polymer matrix; a few of these areas are highlighted by arrows in the Figure. If the local nanotube concentration is high enough, the electric field artifact will be overlaid on the secondary electron image. This explanation is consistent with the theory of electric field artifact imaging described by Goldstein et al. and others (11-14).

TEM studies were hindered by the weak contrast of the SWNTs within the composite, and two methods are used for contrast enhancement with some success. Image math and power spectrum filtering operations are used to enhance the periodicity contrast of the SWNT versus the polymer matrix. The adhesion and wetting of a polymer matrix on SWNT surfaces is assessed using energy filtered TEM (EFTEM) and electron energy loss spectroscopy (EELS) techniques (15).



In the SPM techniques contrast is generated by the paramagnetic and electrical behavior of the SWNTs (16). Direct imaging of SWNT bundles and even individual tubes is achieved with the SPM technique of magnetic force microscopy (MFM). The MFM technique is an interleaved atomic force microscopy (AFM) procedure using a cantilever coated with a ferromagnetic material, typically cobalt. The AFM probe records the sample topography in a standard intermittent contact mode, then the probe is lifted a fixed distance above the recorded surface features and long range forces are measured as a phase shift on the freely oscillating cantilever. Tunneling AFM (TUNA) permits visualization of the percolation network by mapping local current flow from a sample and probe operating under a bias potential. This is similar to current sensing AFM (CAFM) but operates in the pA range.

## 5.4 Suggested Protocol

The investigation of 4 samples is described to illustrate the characterization procedure (see Table 5.1). It is important to note that the samples are all SWNT-polyimide composites made under various processing conditions or with varying concentrations of nanotubes. Details of sample preparation are documented elsewhere (1, 2, 3, 15).

Characterization of SWNT dispersion is performed in a top down approach. Optical microscopy is used as a screening tool for electron and probe microscopy. Table 5.1 shows an example of the optical microscopy images taken in transmission for each sample.

The samples are each prepared for optical microscopy by either casting a film or preparing a thin section. If the sample is transparent, transmission illumination is a very good and quick method to capture the large-scale bulk dispersion. For a uniformly dispersed composite, at least  $\times 200$  magnification is recommended. Agglomerations on a scale large than  $1\ \mu\text{m}$  are easily visible with this technique. If the sample is not transparent, illumination via reflection does give some indication of the large-scale dispersion but the sample will need to be examined on the surface and in cross-section to assess the dispersion throughout the bulk of the sample.

Sample 1 was processed in a direct mixing procedure and large-scale agglomerates could be clearly seen. The percent optical transmission of this sample is very low, on the order of 1 % at 500 nm. Sample 2 was made with the same formulation but the nanotubes were incorporated into the composite via an in-situ polymerization technique (1, 3). In contrast to the direct mixing technique, this sample has a 32 % transmission at 500 nm with the same thickness.



Sample 2 is considered “optically dispersed.” If the composite does not need further optimization for the intended application, optical characterization is usually sufficient. However, if optimization of mechanical, electrical, or thermal properties is required, a more in-depth analysis of the dispersion is needed.

Samples 2, 3, and 4 illustrate the need for characterization beyond the optical microscope. These samples are all considered optically dispersed though they have different mechanical and electrical properties. It is rationalized that the resulting differences in mechanical and electrical properties are due to varying levels of dispersion of the SWNTs within the composite. Differences in samples 2, 3 and 4 are visible with optical microscopy but it is not clear what is the cause of the differences. Scratches, dust, entrapped air bubbles and catalyst particles along with nanotube agglomerates are visible in all the images. These defects are clearly visible with this technique and need to be recorded to give an overview of the nanotube distribution and the overall defect density. What is not clear is how the majority of the tubes are distributing themselves between these defects.

To investigate the difference between samples 2, 3 and 4 beyond the optically dispersed limit requires an investigation of the nature of the dispersion below the 1  $\mu\text{m}$  scale. The main tool employed in this investigation is the high resolution FE-SEM (HR-FESEM). This tool creates a stable electric field in most polymers and generates a very high collection efficiency of the secondary electrons, such that samples just exceeding the electrical percolation threshold are easily imaged without the typical thin metal coating. Figure 5.4 shows samples (1 to 4) normal to the film surface and in cross-section. Aggregates and an inhomogeneous distribution are visible in the film and cross-section of samples (1 to 3), whereas a uniform distribution with no visible aggregation is seen in sample 4. At this point it is important to note that the only difference between samples 3 (Figures 5.4e and 5.4f) and 4 (Figures 5.4g and 5.4h) is the SWNT manufacturing process. Sample 3 was made by the HiPco process and sample 4 was made by a laser ablation technique. The HR-FESEM is powerful enough to detect the dispersion differences due only to the SWNT manufacturing process.

The electron microscopy investigations of these composites requires very little preparation. Samples are mounted on the specimen stage using a conductive adhesive, typically a silver paste. It is important that the imaging surface has at least a moderate conductivity ( $>10^{-8}$  S/cm). The samples are not coated with a conductive layer, but rather inserted directly into the specimen chamber without any additional preparation. The accelerating voltage of the primary electron beam is set to as low of a voltage as is practical for imaging the specimen.

Typically this process begins somewhere around 0.5 keV and is brought up until a contrast is generated between the conductive nanotubes and the non-conducting host matrix. If contrast cannot be established, a variation in the scan rate may be necessary to establish the contrast.

The ability to image a network of nanotubes is not limited to HR-FESEM. Conventional W-filament SEMs are more than capable of imaging such networks as shown in Figure 5.5. Typically, great efforts are employed to reduce the presence of such image artifacts, as those arising from a charge build-up that generates a large electric field. However, for these studies the electric field artifact is the tool exploited to image nanotubes that are part of the percolation network. Thus uncoated SWNT-polymer composite samples are directly inserted into the electron microscope and grounded to a sample stage with silver paste. With SEM, details on SWNT aggregation and distribution are easily determined and estimates of the bundle sizes can be made as well.

More quantitative information on the size of individual tubes and how they bundle requires the use of the TEM. SWNT-polymer composite samples typically require microtoming or ion milling to create thin sections suitable for TEM imaging. Figure 5.6 shows a SWNT-polymer composite where the individual tubes in bundles are clearly visible in the polymer under high magnification. It was observed that the tubes were not locked into a single rope-like configuration, but pass from one bundle to the next.

Novel scanning probe techniques are shown in Figure 5.7. MFM characterized the dispersion of the SWNT in polymer composites by mapping the magnetic field at a fixed height above the sample (16). The TUNA technique was complementary to MFM, though much more straightforward. These SPM techniques are of particular interest because they are simple approaches that do not require an electron microscope. The distribution of SWNTs in the polymer matrix are clearly visible in both the MFM (Figure 5.7(b, d)) and TUNA images (Figure 5.7(c, e)) (21).

The MFM requires the use of a Co/Cr coated AFM cantilever. Contrast is enhanced with the thicker Co coatings found on high moment MFM cantilevers ( $\approx 100$  nm Co). These thick coatings increase the radius of the MFM tip and degrade the spatial resolution. Careful consideration of spatial resolution versus contrast generation needs to be balanced for the MFM imaging. Once a suitable cantilever that gives adequate contrast and spatial resolution is found, the MFM probe is magnetized by placing the probe over a strong magnet for several minutes. The sample is then placed on the scanner above a strong magnet. The paramagnetic nanotubes, which are a subset of the total nanotube

population, disrupt the local magnetic field from the strong magnet under the sample. These nanotubes are imaged with the MFM in an interleave mode. The sample topography is first scanned and then the probe is raised a fixed distance, typically (7 to 15) nm, above the surface and the magnetic field gradient is then recorded. These small lift heights require that the sample be relatively flat before imaging. Thin films formed by spin casting or knife coating work best.

The TUNA procedure requires the use of a conductive AFM probe. The restrictions on the coatings are limited so long as the probe is conductive. As such the conductive probes can have a much sharper tip radius when compared to the MFM probes. The TUNA procedure is also a direct technique, not requiring an interleave or lift mode. The sample topography and tunneling current are recorded simultaneously at each pixel. Additionally, the bias voltage can be scanned to enhance or reduce contrast in the current image. This scanning of the bias voltage can even bring different portions of the network into view, allowing for a more detailed analysis of the network as a function of applied voltage.

### 5.5 Conclusions

The use of conventional microscopy techniques enables the investigation of carbon nanotube dispersions in polymer composites. Subtle differences at the nanoscale produce large changes in the composite and necessitate the closer examination of these materials by electron and probe microscopy. The end result is a method of SWNT composite investigation that involves examination by optical microscopy to first determine if SWNT dispersion is poor. Second, the SEM is used on the composite surface and cross-section to determine bulk dispersion. If additional information is required beyond the degree of dispersion, then direct imaging of the nanotubes by TEM yields information on the size and packing of individual bundles. The use of FE-SEM over conventional SEM is not necessary to assess the dispersion, but it can be beneficial for composites with limited conductivity or samples susceptible to significant beam damage. Probe microscopy techniques are useful tools to investigate nanotube dispersion and provide complementary information to electron microscopy.

### Acknowledgement

Park appreciates the NASA University Research, Engineering and Technology Institute on Bio Inspired Materials (BIMat) under award no. NCC-1-02037 for partial support.



## Literature Cited

1. Park C, Ounaies Z, Watson KA, Pawlowski KJ, Lowther SE, Connell JW, Siochi EJ, Harrison JS and St. Clair TL 2002. *NASA/CR* 2002-211940
2. Kumar S, Dang TD, Arnold FE, Bhattacharyya AR, Min BG, Zhang X, Vaia RA, Park C, Adams WW, Hauge RH, Smalley RE, Ramesh S and Willis P A 2002. *Macromolecules* 35: 9039
3. Ounaies Z, Park C, Wise KE, Siochi EJ and Harrison J S 2003. *Composites Sci. and Technol.* 63: 1637
4. Siochi EJ, Lillehei PT, Wise KE, Park C and Rouse JH 2003. *SEM Annual Conference MEMS/NEMS*
5. Siochi EJ, Working DC, Park C, Lillehei PT, Rouse JH, Topping CC, Bhattacharyya A and Kumar S 2004. *Composites Part B* 35: (5) 439
6. Smith J G Jr., Connell JW, Delozier DM, Lillehei PT, Watson KA, Lin Y, Zhou B and Sun Y-P 2004. *Polymer* 45: 825
7. Delozier DM, Tigelaar DM, Watson KA, Smith JG Jr., Lillehei PT and Connell J W 2004. *SAMPE Symposium & Exhibition*
8. Haggemueller R, Gommans HH, Rinzler AG, Fischer JE and Winey KI 2001. *Chem. Phys. Lett.* 330: 219
9. Thostensona ET, Renb Z and Choua T-W 2001. *Composites Sci. and Technol.* 61: 1899
10. Strano MS, Dyke CA, Usrey ML, Barone PW, Allen MJ, Shan H, Kittrell C, Hauge RH, Tour JM and Smalley RE 2003. *Science* 301: 1519
11. Knoll M 1941. *Naturwissenschaften* 29: 335
12. Kong J, Soh HT, Cassell AM, Quate CF and Dai H 1998. *Nature* 395: 878
13. Zhang Y, Chang A, Cao J, Wang Q, Kim W, Li Y, Morris N, Yenilmez E, Kong J and Dai H 2001. *Appl. Phys. Lett.* 79: 3155
14. Goldstein JI, Lyman C E, Newbury D E, Lifshin E, Echlin P, Sawyer L, Joy D C and Michael J R 2003. *Scanning Electron Microscopy and X-Ray Microanalysis* 3<sup>rd</sup> ed. Kluwer Academic/Plenum Publishers, New York Chapter 5.
15. Park C, Crooks RE, Siochi EJ, Harrison JS, Evans N, Kenik E 2003. *Nanotechnology* 14: L11–L14
16. Lillehei PT, Park C, Rouse JH and Siochi EJ 2002. *Nano. Lett.* 2: 827
17. Viswanathan R and Heaney MB 1995. *Phys. Rev. Lett.* 75: 4433
18. Simpson J, Ounaies Z and Fay C 1997. *Mat. Res. Soc. Symp. Proc.* 459: 53
19. Wise K E, Park C, Siochi EJ, Harrison J S 2004. *Chem. Phys. Lett.* 391: 207
20. St. Clair AK and St. Clair TL 1986. *U.S. Patent* 4,603,061
21. The topographical image and the MFM image were obtained simultaneously, while the TUNA image was taken on the same sample after the tip was exchanged. Thus the MFM and TUNA images are at slightly different locations on the sample.



## Figures and Tables

**Table 5.1.** Optical microscopy images of samples 1-4.

**Figure 5.1.** Guide to assess the dispersion of SWNT in polymer matrices.

**Figure 5.2.** Optical micrographs: (a) undesirable dispersion with SWNT aggregates, (b) desirable uniform SWNT dispersion (optically dispersed) in a polyimide matrix.

**Figure 5.3.** HR-FESEM images of a SWNT-CP2 composite in cross-section showing the SWNTs penetrating out of the film. Nanotubes that are penetrating out of the cross-section generate their own secondary electrons and appear as bright filaments in the image. The arrows highlight points where the nanotubes penetrate into the polymer and disrupt the electric field in the surrounding polymer. The contrast is then reversed and the nanotubes appear as dark regions against the bright polymer matrix.

**Figure 5.4.** HR-FESEM images on the dispersion quality of samples 1-4. (a) Surface and (b) cross-section of sample 1 showing poor dispersion quality. Optical microscopy already showed this sample had a poor dispersion; shown here for comparison. (c) Surface and (d) cross-section of sample 2 showing improved dispersion over the direct mixing technique. (e) Surface and (f) cross-section of sample 3 showing an improved dispersion from using the  $\beta$ -CN polymer. Dispersion is still not ideal due to poor quality of SWNT. (g) Surface and (h) cross-section of sample 4 showing nearly 100 % dispersion, no visible aggregates, very small bundles, and no resin rich areas.

**Figure 5.5.** SEM image of a SWNT-CP2 composite showing the same electric field artifact contrast as seen with the HR-FESEM.

**Figure 5.6.** TEM of SWNT-CP2 directly showing individual tubes in the polymer matrix.

**Figure 5.7.** Scanning probe microscopy images complementary to electron microscopy of 2 SWNT- $\beta$ -CN composites (a-c: 0.5% SWNT  $\beta$ -CN, d-f: 2% SWNT  $\beta$ -CN). (a,d) Topography, (b,e) MFM images and (c,f) TUNA images.

Figure 5.1

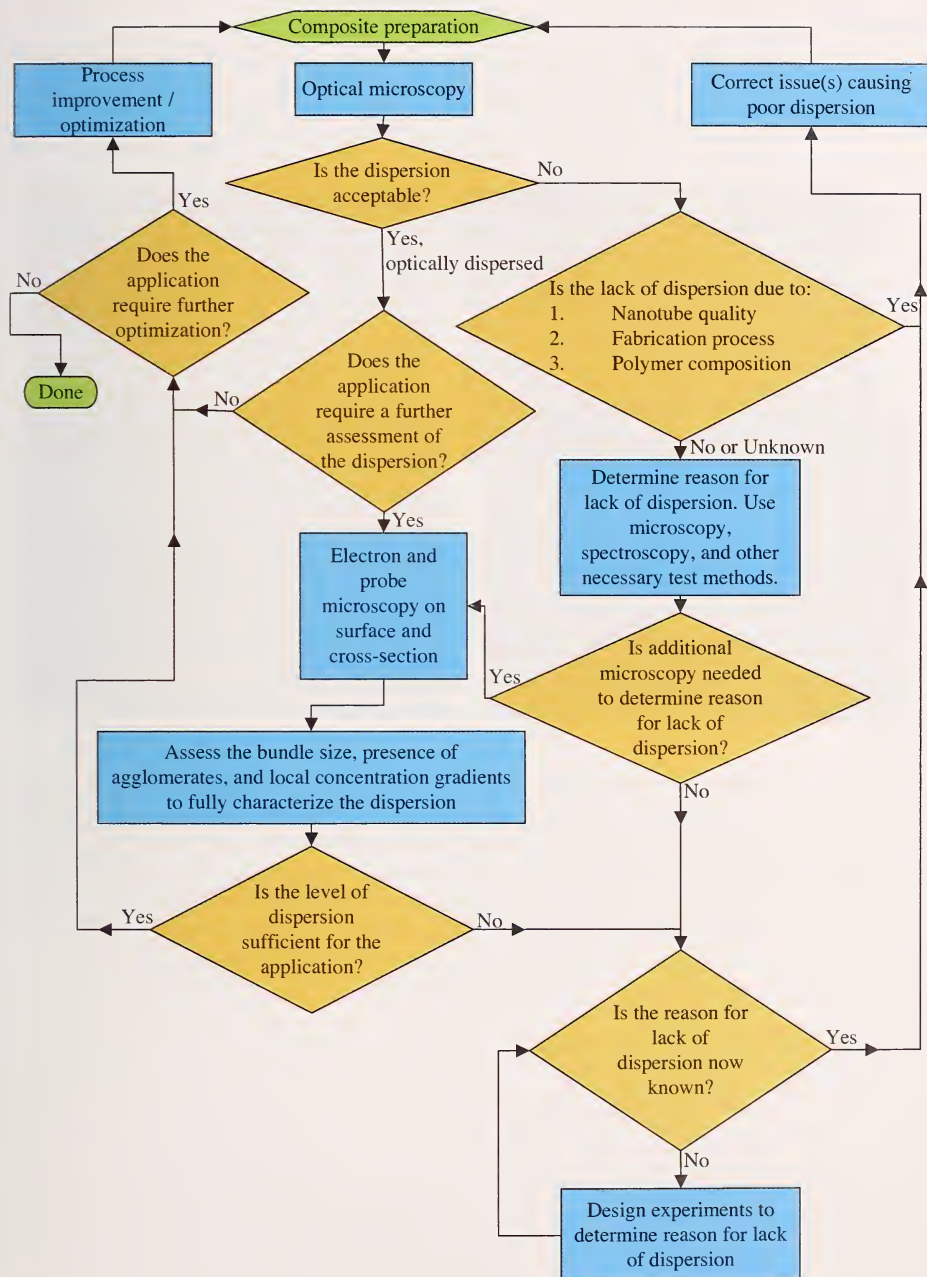
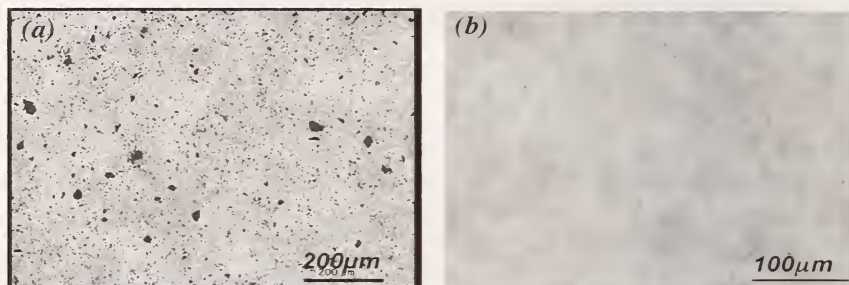


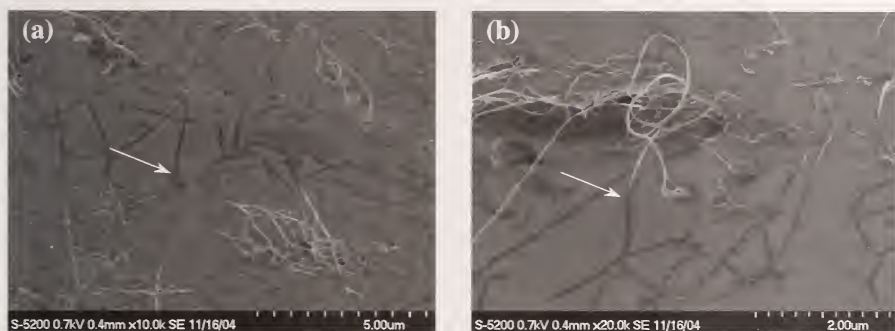
Figure 5.1. Guide to assess the dispersion of SWNT in polymer matrices.

Figure 5.2



**Figure 5.2.** Optical micrographs: (a) undesirable dispersion with SWNT aggregates, (b) desirable uniform SWNT dispersion (optically dispersed) in a polyimide matrix.

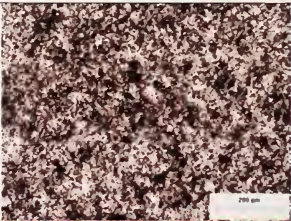

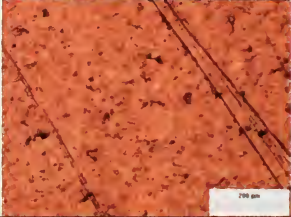
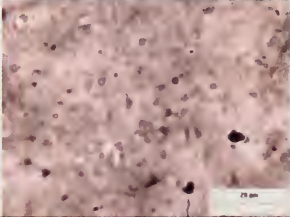

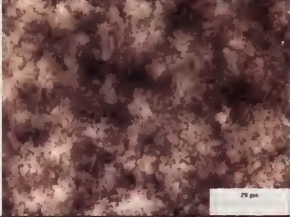

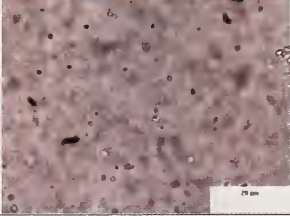
Figure 5.3



**Figure 5.3.** HR-FESEM images of a SWNT-CP2 composite in cross-section showing the SWNTs penetrating out of the film. Nanotubes that are penetrating out of the cross-section generate their own secondary electrons and appear as bright filaments in the image. The arrows highlight points where the nanotubes penetrate into the polymer and disrupt the electric field in the surrounding polymer. The contrast is then reversed and the nanotubes appear as dark regions against the bright polymer matrix.

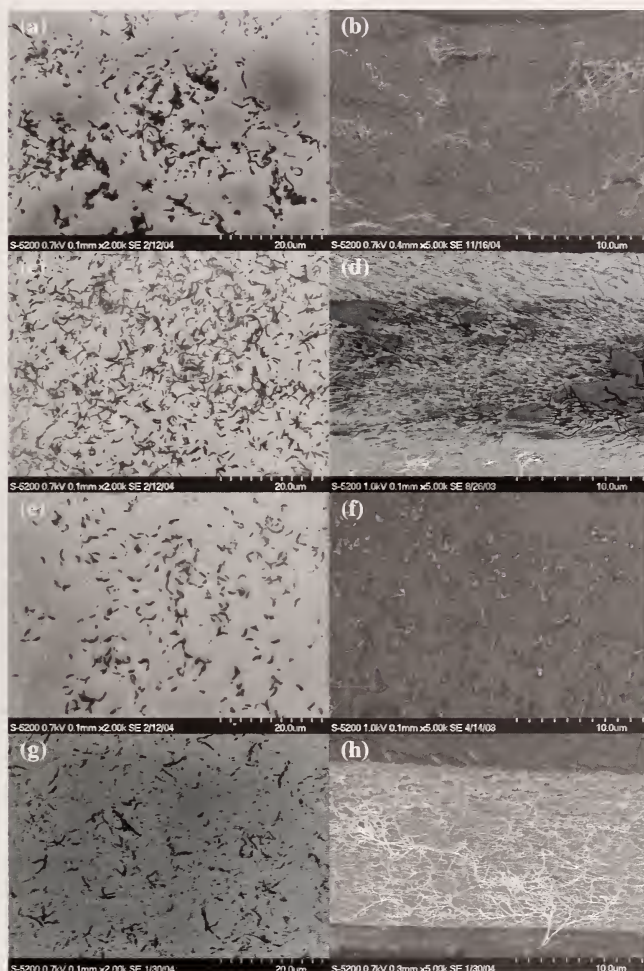


Table 5.1

Sample	Mixing Conditions	Optical Microscopy	
Sample 1 1% SWNT CP2	Direct Mix		
Sample 2 1% SWNT CP2	<i>In-situ</i> polymerization under sonication		
Sample 3 0.5% SWNT $\beta$ -CN	<i>In-situ</i> polymerization with HiPco SWNT		
Sample 4 0.5% SWNT $\beta$ -CN	<i>In-situ</i> polymerization with laser ablation SWNT		

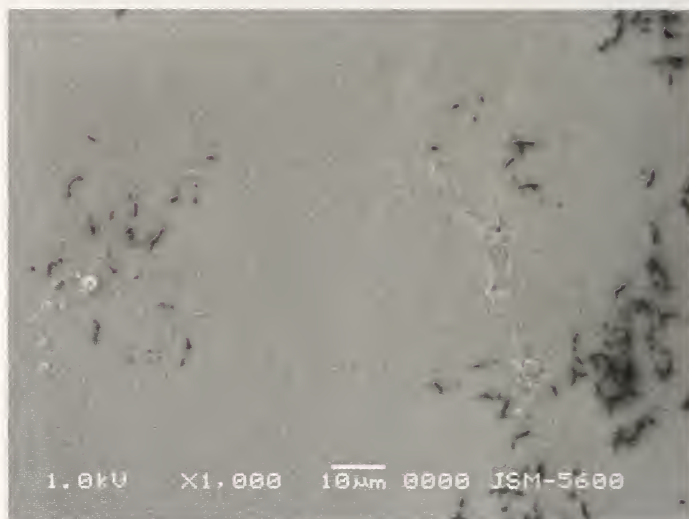
**Table 5.1.** Optical microscopy images of samples 1-4.

Figure 5.4



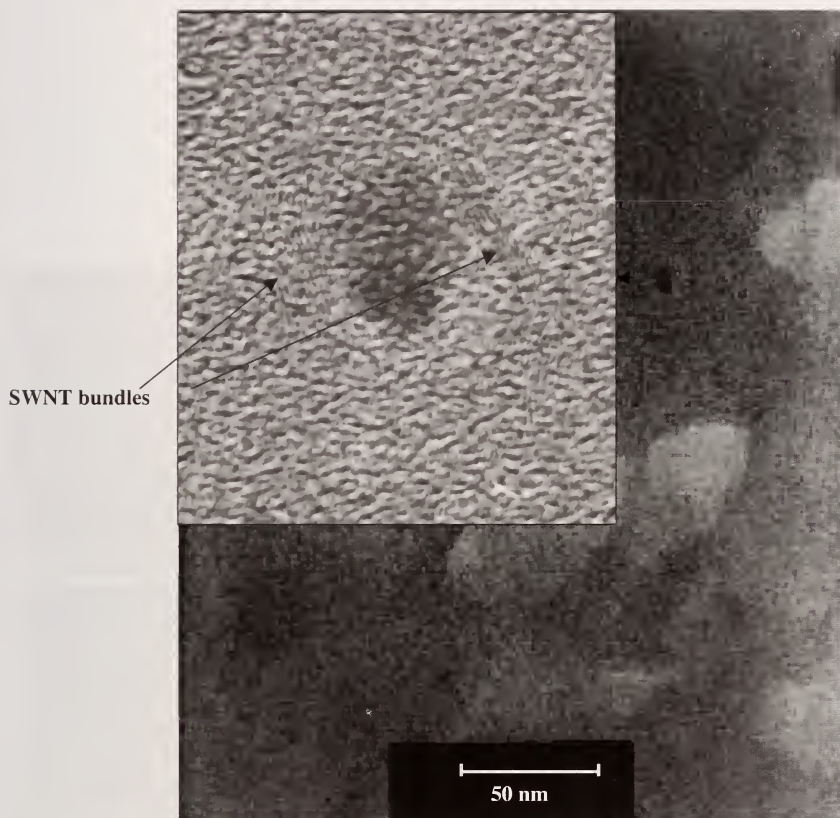
**Figure 5.4.** HR-FESEM images on the dispersion quality of samples 1-4. (a) Surface and (b) cross-section of sample 1 showing poor dispersion quality. Optical microscopy already showed this sample had a poor dispersion; shown here for comparison. (c) Surface and (d) cross-section of sample 2 showing improved dispersion over the direct mixing technique. (e) Surface and (f) cross-section of sample 3 showing an improved dispersion from using the  $\beta$ -CN polymer. Dispersion is still not ideal due to poor quality of SWNT. (g) Surface and (h) cross-section of sample 4 showing nearly 100 % dispersion, no visible aggregates, very small bundles, and no resin rich areas.

Figure 5.5



**Figure 5.5.** SEM image of a SWNT-CP2 composite showing the same electric field artifact contrast as seen with the HR-FESEM.

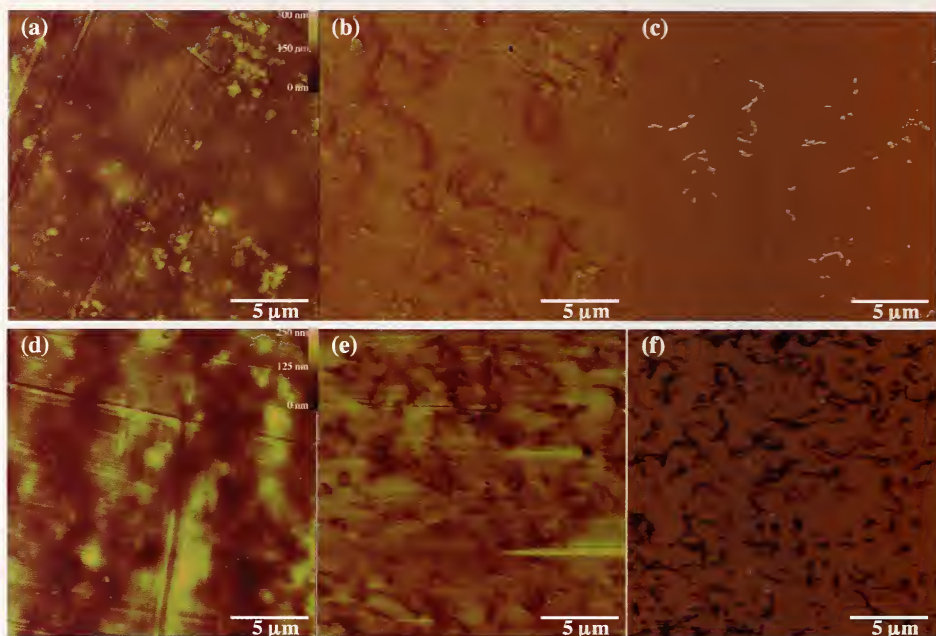
Figure 5.6



**Figure 5.6.** TEM of SWNT-CP2 directly showing individual tubes in the polymer matrix.



Figure 5.7



**Figure 5.7.** Scanning probe microscopy images complementary to electron microscopy of 2 SWNT- $\beta$ -CN composites (a-c: 0.5% SWNT  $\beta$ -CN, d-f: 2% SWNT  $\beta$ -CN). (a,d) Topography, (b,e) MFM images and (c,f) TUNA images.









